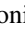











# ALMA Observations of Young Eruptive Stars: Continuum Disk Sizes and Molecular Outflows

Antonio S. Hales<sup>1,2</sup> , Sebastián Pérez<sup>3</sup> , Camilo Gonzalez-Ruilova<sup>4,5</sup> , Lucas A. Cieza<sup>5</sup> , Jonathan P. Williams<sup>6</sup> , Patrick D. Sheehan<sup>2</sup> , Cristián López<sup>1</sup>, Simon Casassus<sup>4</sup> , David A. Principe<sup>7</sup> , and Alice Zurlo<sup>5,8</sup> 

<sup>1</sup> Joint ALMA Observatory, Avenida Alonso de Córdova 3107, Vitacura 7630355, Santiago, Chile; [ahales@alma.cl](mailto:ahales@alma.cl)

<sup>2</sup> National Radio Astronomy Observatory, 520 Edgemont Road, Charlottesville, VA 22903-2475, USA

<sup>3</sup> Departamento de Física, Universidad de Santiago de Chile, Av. Ecuador 3493, Estación Central, Santiago, Chile

<sup>4</sup> Departamento de Astronomía, Universidad de Chile, Casilla 36-D, Santiago 8330015, Chile

<sup>5</sup> Nucleo de Astronomía, Facultad de Ingeniería y Ciencias, Universidad Diego Portales, Av. Ejercito 441, Santiago, Chile

<sup>6</sup> Institute for Astronomy, University of Hawaii, Honolulu, HI 96822, USA

<sup>7</sup> MIT Kavli Institute of Astrophysics and Space Research, 70 Vassar Street, Cambridge, MA 02139, USA

<sup>8</sup> Escuela de Ingeniería Industrial, Facultad de Ingeniería y Ciencias, Universidad Diego Portales, Av. Ejercito 441, Santiago, Chile

Received 2020 April 10; revised 2020 July 3; accepted 2020 July 3; published 2020 August 27

## Abstract

We present Atacama Large Millimeter/submillimeter Array (ALMA) 1.3 mm observations of four young, eruptive star–disk systems at 0''4 resolution: two FUors (V582 Aur and V900 Mon), one EXor (UZ Tau E), and one source with an ambiguous FU/EXor classification (GM Cha). The disks around GM Cha, V900 Mon, and UZ Tau E are resolved. These observations increase the sample of FU/EXors observed at subarcsecond resolution by 15%. The disk sizes and masses of FU/EXors objects observed by ALMA so far suggest that FUor disks are more massive than Class 0/I disks in Orion and Class II disks in Lupus of similar size. EXor disks in contrast do not seem to be distinguishable from these two populations. We reach similar conclusions when comparing the FU/EXor sample to the Class I and Class II disks in Ophiuchus. FUor disks around binaries are host to more compact disks than those in single-star systems, similar to noneruptive young disks. We detect a wide-angle outflow around GM Cha in <sup>12</sup>CO emission, wider than typical Class I objects and more similar to those found around some FUor objects. We use radiative transfer models to fit the continuum and line data of the well-studied disk around UZ Tau E. The line data are well described by a Keplerian disk, with no evidence of outflow activity (similar to other EXors). The detection of wide-angle outflows in FUors but not in EXors support the current picture in which FUors are more likely to represent an accretion burst in the protostellar phase (Class I), while EXors are smaller accretion events in the protoplanetary (Class II) phase.

*Unified Astronomy Thesaurus concepts:* [Protoplanetary disks \(1300\)](#); [Star formation \(1569\)](#); [Stellar accretion disks \(1579\)](#)

## 1. Introduction

Multiepoch accretion outbursts are believed to play a key role in the build-up of the final stellar mass (Hartmann 2008; Hartmann et al. 2016). Episodes of variable accretion are invoked to solve the well-known luminosity problem, in which low-mass stars appear fainter than predictions of steady-state accretion models (Kenyon et al. 1990; Evans et al. 2009). Despite being key to our understanding of low-mass star (and planet) formation, the exact mechanisms that trigger outbursts are still poorly understood, and this topic is of growing interest as observational capabilities at long wavelengths (such as ALMA) have developed (see Audard et al. 2014 for a review).

Outbursting sources have been divided into two classes, FUors and EXors (named after the prototypes FU Ori and EX Lupi, respectively). FUors have large ( $\Delta V_{\text{mag}} \sim 5$ ), long-lived (years to decades) outbursts (Herbig 1966), whereas EXors have moderate ( $\Delta V_{\text{mag}} \sim 2\text{--}4$ ), shorter (days/months) episodes of high accretion. Several observational signatures indicate differences in physical structures and accretion processes of each class, which suggest that FUors and EXors might correspond to different evolutionary stages.

EXors show rich optical and infrared emission lines similar to those of classical T Tauri stars (CTTS), which brighten during the burst, consistent with magnetospheric accretion. They also have spectral energy distributions (SEDs) similar to

those of Class II sources (e.g., Sipos et al. 2009), suggesting these are typical star+disk systems with no detectable remnant envelope. The few available optical spectra of FUors in quiet states show they also resemble those of CTTS (Herbig & Harlan 1971). In outburst, however, FUors show little sign of magnetospheric accretion and instead exhibit optical P-Cygni profiles at H $\alpha$  and sodium lines (indicative of strong winds of  $\sim 10\%$  the accretion rate; Calvet et al. 1993), as well as double-peaked absorption features in some optical and near-IR lines. The extremely high luminosity and spectroscopic features of the prototype FU Orionis itself have been explained in the frame of an accretion disk model in which the disk is internally heated through strong viscous accretion, overwhelming the stellar photosphere (Hartmann & Kenyon 1985, 1996). This explains the high accretion rates and double, differential, absorption lines (with the difference in line profiles explained by absorption at different radii; e.g., Zhu et al. 2009). Most FUors are also associated with reflection nebulae, and many have Class I SEDs with prominent CO outflows observed at millimeter wavelengths, both indicating that they are still partially surrounded by their parent envelope and therefore suggesting a younger evolutionary stage compared to EXors (see Reipurth & Aspin 2010; Hartmann et al. 2016 for review). Objects that share spectroscopic features of FUors, but for which outbursts have never been observed, are called FUor-like objects (see Connelley & Reipurth 2018, for details).

Different mechanisms have been proposed to explain the origin for the outbursts (Audard et al. 2014): disk fragmentation plus the subsequent inward migration of clumps (Vorobyov & Basu 2015), a combination of magnetorotational and gravitational instabilities (Armitage et al. 2001), and enhanced accretion induced by stellar (Bonnell & Bastien 1992) or planetary companions (Lodato & Clarke 2004). The key ingredients to distinguish between the above outburst mechanisms are the total disk mass and the disk spatial structure. However, only a few FU/EXor objects have been recently observed at sufficient angular resolution at millimeter/sub-millimeter wavelengths. Recent surveys with ALMA and the SMA (Cieza et al. 2018; Liu et al. 2018) have shown that 1.3 mm fluxes of the outbursting sources span over three orders of magnitude, but the FUor objects are significantly brighter than the EXor objects and typical Class II disks.

The inferred disk masses for the brightest FUor objects are large enough that they may be gravitationally unstable. Nevertheless, follow-up observations at the 0".03 (12 au) resolution of V883 Ori, the most massive disk in the survey, were unable to identify the predicted signatures of instabilities or fragmentation (e.g., spirals or clumps). The fainter targets are all EXor objects and have low disk masses,  $\sim 1\text{--}5 M_{\text{Jup}}$ , that imply gravitational instability is unlikely to play a role in their outbursts (e.g., Cieza et al. 2018).

Some FUor objects are close binaries with both components hosting disks (e.g., FU Orionis, L1551 IRS, HBC 494; Hales et al. 2015; Cruz-Sáenz de Miera et al. 2019; A. Zurlo et al. 2020, in preparation), whose interaction could help explain the outbursts in some of the systems. Recent ALMA observations of FU Orionis show that the disks are indeed compact in continuum emission (11 au in radius) while the gas kinematics displays extended features, possibly tracing binary and/or intracloud interactions (Pérez et al. 2020).

ALMA spectral line observations of  $^{12}\text{CO}$  show that FUors have active circumstellar environments characterized by strong outflows interacting with larger-scale structure (Kóspál et al. 2017; Ruíz-Rodríguez et al. 2017a, 2017b; Zurlo et al. 2017; Principe et al. 2018; Takami et al. 2019). On the other hand, EXor sources do not show detectable outflows, with the possible exception of V1647 Ori, a system with an unclear FUor/EXor classification (Principe et al. 2018) and EX Lupi itself (around which a small arc-shape feature is detected at  $\sim 2 \text{ km s}^{-1}$  from the systemic velocity; Hales et al. 2018). Although the number of observed sources is small, the differences in outflow activity between FUors and EXors suggest that the two types of objects represent an evolutionary sequence comparable to normal Class I and Class II, respectively. V346 Nor has observational properties more similar to Class 0/I protostars, consistent with the growing number of Class 0 sources discovered to show eruptive behavior (Safron et al. 2015; Johnstone et al. 2018). This suggests that episodic accretion may play an important role even at earlier protostellar stages. Studying the larger-scale structure of eruptive sources is thus crucial for understanding the nature of this common, yet short-lived, high mass accretion variability in young stars.

This work aims to contribute a better understanding of the differences between the two classes of young eruptive stars, FUors and EXors, and how their disk masses, sizes, and associated gas emission compare to those of Class I and Class II protostars. Are FU/EXor disks massive enough to trigger gravitational instability? Do they show the predicted signatures

of a gravitationally unstable disk? Are all variable accretion sources associated with large molecular outflows? For this purpose, we present ALMA observations of four eruptive sources to characterize their distribution of dust and gas and to compare them to those of noneruptive protostars. Section 2 describes our target sample, observations, and data reduction. In Section 3 we present our results, which are discussed in Section 4. Section 5 presents our conclusions.

## 2. Sample Selection and ALMA Observations

### 2.1. Target Sample

There are about  $\sim 38$  known FUor/EXor objects within  $\sim 1$  kpc, of which  $\sim 20$  are observable with ALMA (with decl.  $< +40^\circ$ ; Audard et al. 2014). So far  $\sim 14$  of them have already been observed by ALMA at moderate angular resolution (0".2–0".9; Hales et al. 2015, 2018; Kóspál et al. 2017; Cieza et al. 2018; Cruz-Sáenz de Miera et al. 2019; Takami et al. 2019). In this work, we present ALMA Band 6 observations of four FUor/EXor objects observed in ALMA Cycle 5 (project code 2017.1.01031.S, PI Hales). The targets were selected from the list of Audard et al. (2014) and include two FUors (V582 Aur and V900 Mon), one EXor (UZ Tau E), and one source with ambiguous FU/EXor classification (GM Cha). This apparently small sample represents 10% of known FUor/EXor objects, and these observations increase the number of eruptive sources observed at subarcsecond resolution by 15% (because two of our targets, V900 Mon and UZ Tau E, have already been observed at similar or higher angular resolution; Long et al. 2018; Takami et al. 2019).

V900 Mon is an FUor object discovered by Thommes et al. (2011), who reported a brightening of at least 4 mag in optical magnitude, while follow-up observations indicate the object shows FUor characteristics such as P-Cygni profiles in  $\text{H}\alpha$  and sodium lines, CO absorption in near-IR, as well as an association with a bright, compact reflection nebula (Reipurth et al. 2012). Takami et al. (2019) presented recent ALMA observations that show the presence of a CO outflow and rotating envelope.

V582 Aur is a young eruptive system first identified due to an optical brightening of  $\sim 4$  mag that took place sometime between 1982 and 1986, followed by the appearance of a nebula that was not visible in previous optical images (Samus 2009). Semkov et al. (2013) studied the optical photometry and spectra, and showed that the star has spectroscopic signatures typical of FUors, although some of the color changes have similarities with UXor-type stars (UXors are young stars that show stochastic variability than can be explained by eclipses due to dust fragments in their circumstellar disks; Grinin et al. 2019). Ábrahám et al. (2018) studied the color variations of V582 Aur and suggest that the two 1 yr long dips seen in 2012 and 2017 in the light curve are due to variable extinction rather than enhanced accretion, and therefore more similar to UXors than to FUor/EXors. Zsidi et al. (2019) combine optical and near- and mid-infrared photometry to investigate the physical structure of the dust responsible for the dimming. Millimeter observations with IRAM 30 m and Northern Extended Millimeter Array (NOEMA) reveal a compact continuum source at the position of V582 Aur, together with other clumps in both continuum and CO isotopologs (Ábrahám et al. 2018).

GM Cha (ISO-Cha I 192) is a Class I/II source located in the Chameleon I dark cloud (Moody & Stahler 2017;

**Table 1**  
Summary of ALMA Observations (This Work)

Name	Execution Block	N Ant.	Date	ToS (s)	Avg. Elev. (deg)	Mean PWV (mm)	Phase rms (rad)	Baseline (m)	AR (")	MRS (")
V582 Aur	uid://A002/Xd248b5/X4ff9	41	2018 Sep 22	989	30.3	0.2	0.435	15.1–1397.8	0.3	3.6
V900 Mon	uid://A002/Xd23397/Xe02d	43	2018 Sep 21	1128	75.4	0.2	0.411	15.1–1397.8	0.3	3.7
UZ Tau	uid://A002/Xd23397/X41f6	47	2018 Sep 20	1273	31.2	0.4	0.472	15.1–1397.8	0.3	3.8
GM Cha	uid://A002/Xd28a9e/X4a7b	43	2018 Sep 27	1417	36.4	1.5	0.498	15.1–1397.8	0.3	3.6
GM Cha	uid://A002/Xd29c1f/X5b5e	43	2018 Sep 29	1445	36.3	1.0	0.458	15.1–1397.8	0.2	3.3

**Note.** Summary of the new ALMA observations presented in this work, including number of antennas, total time on source (ToS), target average elevation, mean precipitable water vapor column (PWV) in the atmosphere, phase rms measured on the bandpass calibrator, minimum and maximum baseline lengths, expected angular resolution (AR), and maximum recoverable scale (MRS).

Mottram et al. 2017). The source has no optical counterpart, is located in a region of high extinction (Jones et al. 1985), and is associated with a  $^{12}\text{CO}$  outflow (Mattila et al. 1989; Mottram et al. 2017). From 1996 to 1999, the  $K_s$ -band magnitude increased by 2 mag (Persi et al. 2007), and there is evidence of possible elongated infrared nebulosity in the direction of the outflow. As with V1647 Ori, the observational characteristics of GM Cha are similar to both FUors and EXors. The SED can be well described by a star+disk+infalling envelope and the presence of a reflection nebula suggests similarities with FUors. However, it shows no  $2.3\ \mu\text{m}$  CO band head (neither in absorption nor emission), and the derived accretion rate of  $10^{-7}\ M_{\odot}\ \text{yr}^{-1}$  is three orders of magnitude lower than those of FUors (Persi et al. 2007).

UZ Tau is a well-studied quadruple system, containing a spectroscopic binary with a separation of  $\sim 0.03$  au (Mathieu et al. 1996) surrounded by a large circumbinary disk (UZ Tau E; Tripathi et al. 2018), and another M3+M3 binary pair with a  $0''.34$  ( $\sim 48$  au) projected separation (UZ Tau W). The UZ Tau E continuum disk was imaged by Long et al. (2018) at  $0''.13 \times 0''.11$  resolution and found the presence of at least three sets of rings spanning from 0 to  $\sim 100$  au with one clearly defined gap at 69 au. UZ Tau E shows moderate ( $\sim 1$  mag) short-term variability in the optical and infrared and exhibits characteristics of an EXor (Lorenzetti et al. 2007). Jensen et al. (2007) showed that the periodic variability of UZ Tau E could be explained by the variable accretion caused by interactions between the binary orbit and the circumbinary disk. Czekala et al. (2019) used ALMA data of  $^{13}\text{CO}$  and  $\text{C}^{18}\text{O}$  to study the degree of alignment of the binary and the circumbinary disk, and determined that the disk and the stars are nearly coplanar, which may imply that planets formed in this system will also be coplanar.

## 2.2. Observations

ALMA observations of these four targets were acquired between 2018 September 20 and 29 using the Band 6 receiver ( $\sim 230$  GHz). The total number of available 12 m antennas ranged from 41 to 47, providing baselines ranging from 15.1 m to 1.397 km. A summary of the observations such as precipitable water vapor column (PWV) in the atmosphere, phase rms, target elevation and time on source (ToS), number of antennas, expected angular resolution (AR), and maximum recoverable scale (MRS) is presented in Table 1. Standard observations of bandpass, flux, and phase calibrators were also included.

The spectral setup was chosen to target the  $^{12}\text{CO}(2-1)$ ,  $^{13}\text{CO}(2-1)$ , and  $\text{C}^{18}\text{O}(2-1)$  transitions of carbon monoxide (rest frequencies of 230.538 GHz, 220.399 GHz, and 219.560 GHz,

respectively). The ALMA correlator was configured in Frequency Division Mode to provide spectral resolutions of  $0.09\ \text{km}\ \text{s}^{-1}$ . Two spectral windows in Time Division Mode (TDM) to image dust continuum were set up at central frequencies of 218.0 and 233.0 GHz, each with total bandwidths of 1.875 GHz.

## 2.3. Data Reduction

All data were calibrated using the ALMA Science Pipeline (version 40896 Pipeline-CASA51-P2-B) in CASA 5.1 (CASA<sup>9</sup>; McMullin et al. 2007) by staff at the North American ALMA Science Center. The Pipeline uses CASA tasks to perform the data reduction and calibration in a standard fashion, which includes correction for Water Vapor Radiometer and system temperature, as well as bandpass, phase, and amplitude calibrations.

Imaging of the continuum and molecular emission lines was performed using the TCLEAN task in CASA. The two continuum spectral windows were imaged together using Briggs weighting with a robust parameter of 0.5, resulting in a final continuum image centered at 225.5 GHz. The synthesized beam size achieved for each target is shown in Table 2. Because all targets are bright enough for self-calibration, a single iteration of phase-only self-calibration was performed to improve coherence. The resulting continuum sensitivity achieved for each target is shown in Table 2.

Imaging of the spectral lines was performed using TCLEAN on the continuum-subtracted data (which was subtracted using CASA task UVCONTSUB). Self-calibration tables from the continuum data were applied to the spectral line data before imaging the CO lines. During TCLEANing the spectral channels were binned to  $0.3\ \text{km}\ \text{s}^{-1}$  for UZ Tau E and to  $0.5\ \text{km}\ \text{s}^{-1}$  for the other sources. TCLEAN was run with natural weighting to enhance sensitivity.

## 3. Results

### 3.1. Continuum

All observed targets are detected at a high signal-to-noise ratio in continuum emission (Figure 1). We use the CASA task IMFIT to fit an elliptical Gaussian to the images and derive emitting region sizes (deconvolved from the beam) and dust continuum fluxes. We use these sizes as a proxy for the disk radius. The disk sizes are thus estimated from the deconvolved Gaussian FWHM/2 (see Section 4.1 for a discussion on the reliability of this method for estimating disk sizes). The disks around GM Cha and UZ Tau E are resolved. V900 Mon is marginally resolved, as can be seen by inspecting the

<sup>9</sup> <http://casa.nrao.edu/>



**Table 2**  
Summary of Continuum Disk Detections

	V582 Aur	V900 Mon	UZ Tau E	GM Cha
Object type	FUor	FUor	EXor	FU/EXor
$L_{\text{Bol}}(L_{\odot})$	...	106	1.7	>1.5
Companions	...	N	Y (SB+4'')	Y (10'')
$F_{1.3 \text{ mm}}$ (mJy) <sup>a</sup>	$5.3 \pm 0.6$	$9.8 \pm 0.1$	$134 \pm 1$	$10.4 \pm 0.1$
Major axis (mas) <sup>b</sup>	...	$72 \pm 11$	$668 \pm 20$	$613 \pm 8$
Minor axis (mas) <sup>b</sup>	...	$60 \pm 20$	$396 \pm 22$	$221 \pm 2$
Position angle (deg)	...	$164 \pm 63$	$90 \pm 4$	$27.8 \pm 0.3$
Disk radius (au)	...	54	44	49
Inclination (deg)	...	50	59	70
Distance (pc)	2575	1500	131	192
$M_{\text{dust}}(M_{\oplus})$ for $T = 20$ K	1055	662	69	11
$M_{\text{dust}}(M_{\oplus})$ for $T = 60$ K	291	182	19	3
$M_{\text{disk}}(M_{\text{Jup}})$ for $T = 20$ K	332	208	22	3
Peak (mJy beam <sup>-1</sup> )	4.2	9.4	54.7	5.9
rms (mJy beam <sup>-1</sup> )	$1.41 \times 10^{-1}$	$5.23 \times 10^{-2}$	$8.08 \times 10^{-2}$	$3.56 \times 10^{-2}$
Beam Major axis (")	0.49	0.35	0.57	0.57
Beam Minor axis (")	0.28	0.32	0.34	0.37
Beam Position angle (deg)	153.2	77.5	-40.1	17.2

**Notes.** Disks are sorted by declining disk mass. Object type, spectral type, and  $L_{\text{Bol}}$ . Companions are taken from Audard et al. (2014). Distances are obtained from the second data release (DR2) of Gaia (Gaia Collaboration et al. 2018), except for GM Cha, for which we adopt the distance to Cha I from Dzib et al. (2018).

<sup>a</sup> Uncertainties on the continuum flux do not include the absolute flux uncertainty of ALMA.

<sup>b</sup> Deconvolved disk sizes reported by IMFIT.

visibilities (shown in the right panel of Figure 1). V582 Aur, being significantly more distant, is unresolved. The large circumbinary disk around UZ Tau E is resolved, while the individual disks around each component of UZ Tau W are marginally resolved. The derived disk parameters are presented in Table 2. The inclinations are derived from the ratio of the deconvolved minor and major axes. The 225.5 GHz flux for UZ Tau E is consistent with the CARMA measurement of  $131 \pm 6$  mJy (Tripathi et al. 2018), as well as with the 0''.12 resolution ALMA observations ( $129.5 \pm 0.2$  mJy; Long et al. 2018). The disk radius we derive for V900 Mon (54 au) is consistent with the 45 au value inferred by Takami et al. (2019) with a factor of  $\sim 2$  better spatial resolution.

The 1.3 mm photometry of each disk is listed in Table 2. These fluxes will be used to estimate dust masses using the optically thin approximation in Section 4.1 along with a discussion of the key assumptions and their caveats.

### 3.2. Spectral Line Data

Spectral line emission ( $J = 2-1$ ) from the three main isotopologs of CO was detected in all sources. Takami et al. (2019) recently presented a study of V900 Mon in similar spectral transitions, and a detailed analysis of the spectral line data for GM Cha will be presented in a separate paper (C. Gonzalez-Ruilova et al. 2020, in preparation). Therefore, in this work, we present the  $^{12}\text{CO}$  data for all four sources for comparison purposes, and the complete line data ( $^{12}\text{CO}$ ,  $^{13}\text{CO}$  and  $\text{C}^{18}\text{O}$ ) only for UZ Tau E and V582 Aur.

Integrated line emission (moment 0) maps for  $^{12}\text{CO}$  are shown in Figure 2. The total integrated line emission per molecule for UZ Tau E and V582 Aur are presented in Table 3. The moment maps and the final integrated line fluxes are all computed by integrating the channel with emission above  $3\sigma$  and correspond to the velocity ranges annotated in Figure 2. The spectral profiles for UZ Tau E and V582 Aur (integrated over the circular apertures shown in Figure 2) are shown in Figure 3. Figure 4 shows

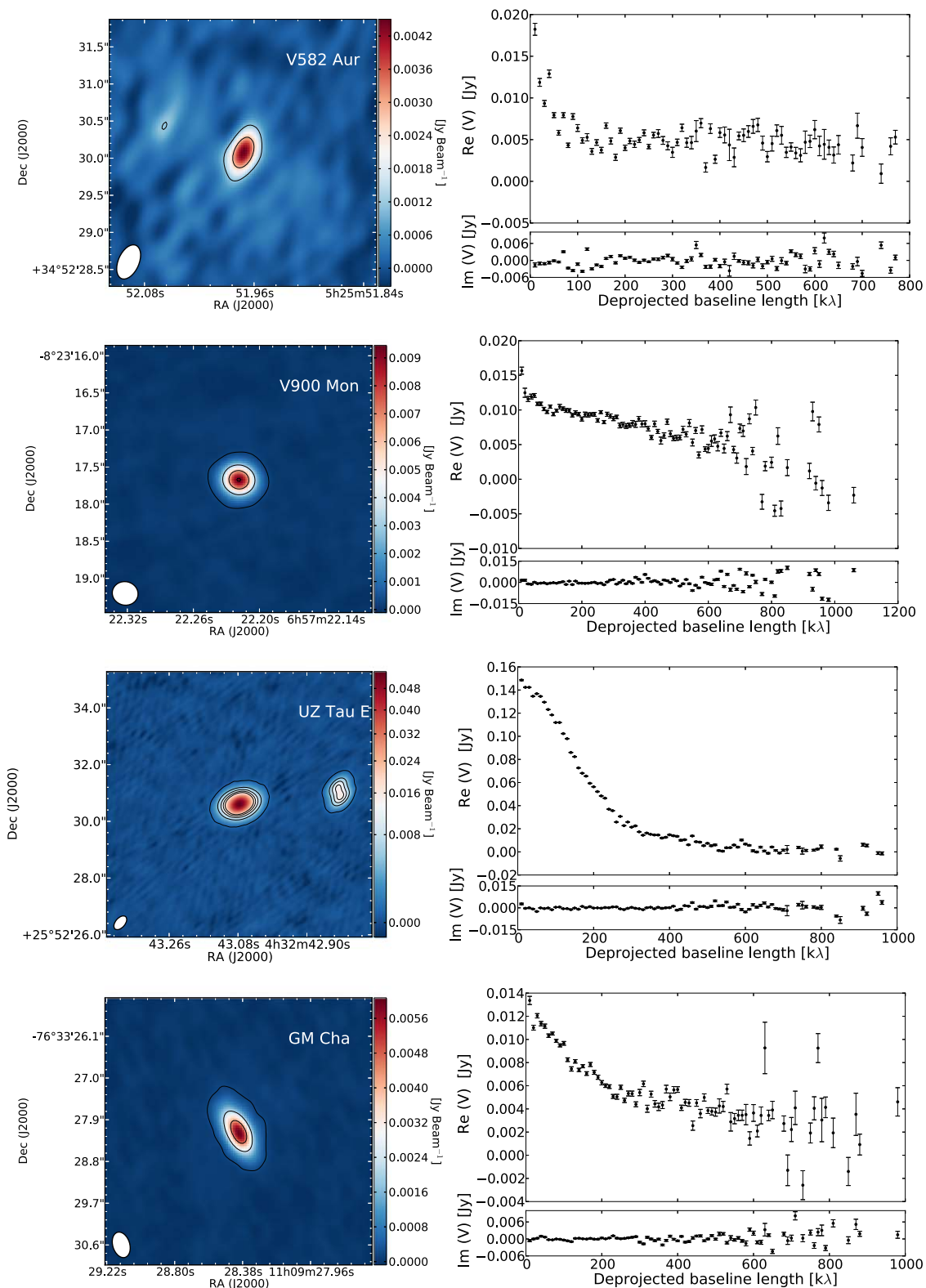
**Table 3**  
Measured CO  $J = 2-1$  Integrated Fluxes (Angular Integrated Intensity)

Source	$^{12}\text{CO}$	$^{13}\text{CO}$	$\text{C}^{18}\text{O}$
UZ Tau	$7.02 \pm 0.02$	$1.16 \pm 0.02$	$0.42 \pm 0.01$
V582 Aur	$5.51 \pm 0.09$	$2.83 \pm 0.07$	$0.81 \pm 0.035$
V900 Mon	$5.06 \pm 0.02$	$3.77 \pm 0.02$	$1.65 \pm 0.02$
GM Cha	$36.03 \pm 0.04$	$3.67 \pm 0.02$	$0.52 \pm 0.01$

**Note.** Integrated line fluxes are in units of mJy km s<sup>-1</sup>. Errors do not include the absolute flux uncertainty, which is estimated to be between 7% and 10% in band 6.

intensity-weighted velocity field (moment 1) images in  $^{12}\text{CO}$ ,  $^{13}\text{CO}$  and  $\text{C}^{18}\text{O}$  for UZ Tau E. Velocity maps showing each CO isotopolog for V582 Aur are presented in Appendix C, together with moment 0 maps of  $^{13}\text{CO}$  and  $\text{C}^{18}\text{O}$ .

All sources show very different morphologies in their  $^{12}\text{CO}$  emission. While the UZ Tau E disk shows a clear Keplerian rotation pattern, V900 Mon and more noticeably GM Cha both show conical cavity walls similar to those detected around other FUors (Figure 5). The V582 Aur  $^{12}\text{CO}$  moment 0 map shows widespread emission and at least three peaks in its spectrum. This is due to its association with a star-forming filamentary cloud with velocities spanning  $[-12.5, -7.5]$  km s<sup>-1</sup> (Ábrahám et al. 2018; Dewangan et al. 2018). The ALMA  $^{12}\text{CO}$  data show compact emission within  $\sim 1''.4$  (3500 au) from the position of the FUor at velocities between  $[-12.85, -11.5]$  km s<sup>-1</sup> for  $^{12}\text{CO}$  and  $[-12.10, -11.5]$  km s<sup>-1</sup> for  $^{13}\text{CO}$ , before cloud contamination becomes dominant (see full channel maps in Appendix C). Central emission near V582 Aur in  $^{13}\text{CO}$  and  $\text{C}^{18}\text{O}$  was previously reported (Ábrahám et al. 2018) using NOEMA. Because of its location close to the source and velocities farther away from the main cloud velocities, it is possible that this central emission is associated with the FUor.



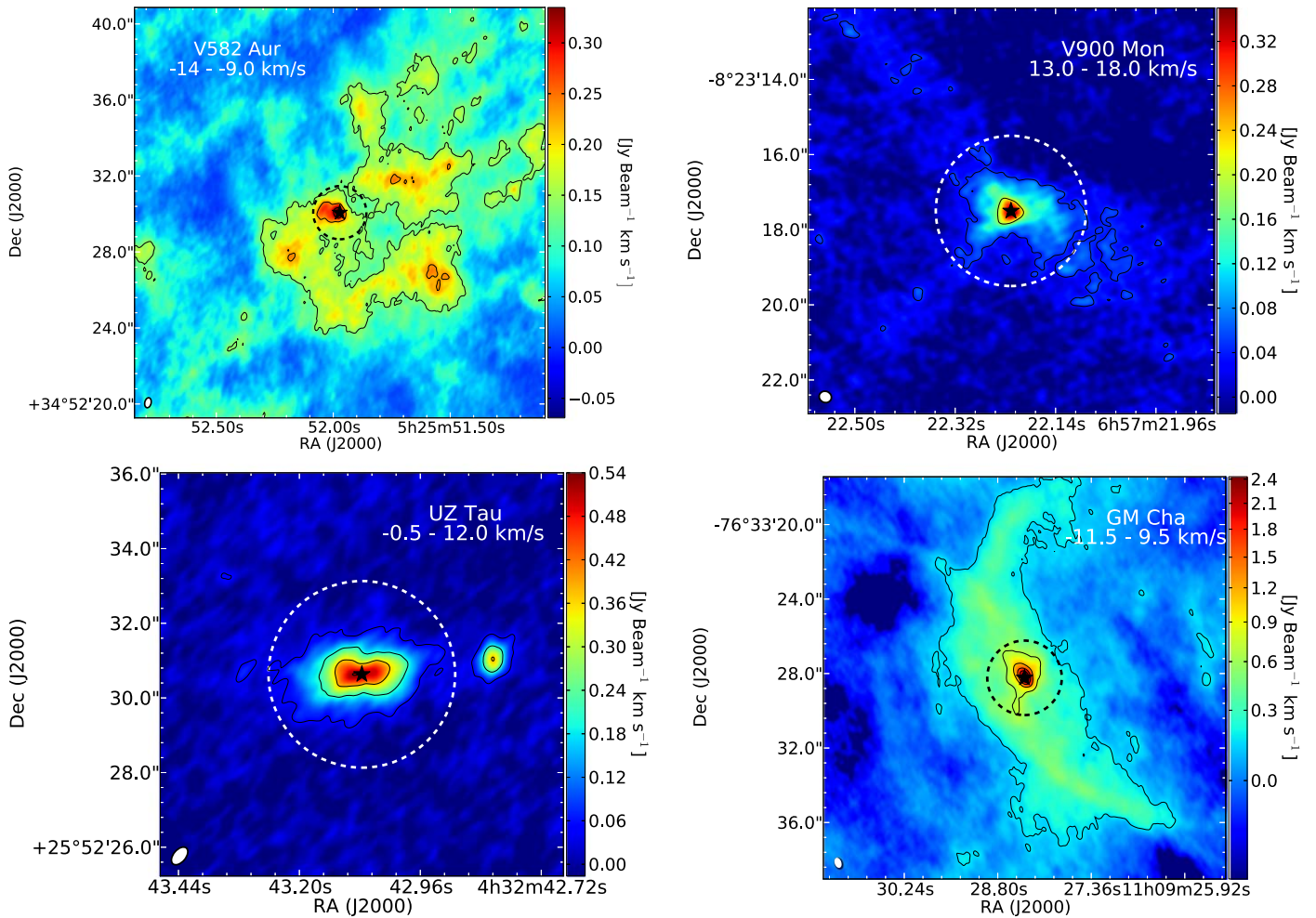
**Figure 1.** Left: ALMA 1.3mm continuum images for the FUor (top) and EXor (bottom) sources. Contour levels for V900 Mon, UZ Tau, and GM Gha start at  $5\sigma$  and increase in steps of  $5\sigma$ , and in steps of  $10\sigma$  for V582 Aur. The synthesized beam size achieved for each target is shown in the lower left. Right: averaged continuum visibilities.

## 4. Discussion

### 4.1. Disk Masses

A crude estimation of the disk dust masses can be obtained under the standard assumption that the continuum emission

from disks is optically thin at millimeter wavelengths (e.g., Hildebrand 1983). This is certainly not true in the disk inner regions (usually in the inner 5–10 au), but it is considered to be a reasonable assumption for the rest of the disk (e.g., Cieza et al. 2018).



**Figure 2.**  $^{12}\text{CO}$  integrated intensity maps (moment 0) for all targets. The dashed circles show the region used to compute the integrated line emissions listed in Table 3. The peak position of the continuum is shown with a star.

We estimate the disk dust masses from the optically thin assumption that relates the observed flux,  $F_\nu$ , to the mass of solids (e.g., Beckwith et al. 1990) via

$$M_{\text{dust}} = \frac{F_\nu d^2}{\kappa_\nu B_\nu(T)}, \quad (1)$$

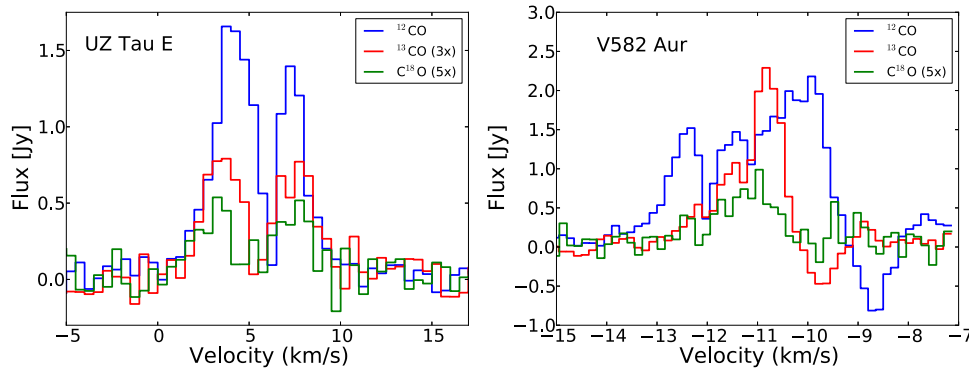
where  $B_\nu$  is the Planck function for a given temperature  $T$ ,  $\kappa_\nu$  is the dust opacity, and  $d$  is the distance to the emitting dust. We note that, at millimeter frequencies, the low temperatures of some disks ( $<100$  K) imply that the Rayleigh–Jeans regime is not ideal for approximating the Planck function. For example, at  $T = 20$  K and  $\nu = 225$  GHz, there is a 30% difference between calculating the full Planck function and the Rayleigh–Jeans approximation. Therefore, caution must be taken when employing the linear temperature dependence offered by the Rayleigh–Jeans approximation.

As discussed in Cieza et al. (2018), the assumption of optically thin emission will underestimate the total dust mass, while the assumption of a temperature of 20 K may overestimate the mass if the dust is warmer; therefore, the two effects may partially offset each other (because the total mass approximately scales as the inverse of temperature). To what extent this statement is valid may depend on the properties of each object. For instance, because FUor sources can be  $\sim 100$

times more luminous than normal stars in Class II disks, one would expect the average temperature of disks in FUor sources to be a factor of  $\sim 3$  higher than in normal Class II disks (because the disk temperature scales with the stellar luminosity  $T \propto L^{1/4}$ ; Chiang & Goldreich 1997). This will result in an overestimation of the disk mass by a similar amount. On the other hand, the more massive and/or compact disks become very optically thick in their inner regions, and therefore, the optically thin assumption will underestimate the total dust mass (e.g., Liu et al. 2019). In the case of V833 Ori, Cieza et al. (2018) found that the total dust mass obtained using the optically thin approximation is similar to the mass derived using radiative transfer, which takes into account the high optical depth in the disk inner regions. However, for HBC 494 and V2775 Ori, they found that the assumptions of optically thin emission and 20 K dust temperature overestimate the mass by a factor of  $\sim 2$  when compared to the radiative transfer results. This can be attributed to the fact that the disks around HBC 494 and V2775 Ori are more compact than the disk around V833 Ori, and therefore, the average disk temperatures are likely higher than 20 K. This highlights the need for combining resolved images with radiative transfer techniques in order to infer the true properties of these disks.

Here we use the dust opacity of Beckwith et al. (1990), i.e.,  $\kappa_{1.3 \text{ mm}} \approx 0.022 \text{ cm}^2 \text{ g}^{-1}$ , to compute dust masses from the fluxes and distances listed in Table 2. We list calculations





**Figure 3.** Integrated spectra for UZ Tau E and V582 Aur in  $^{12}\text{CO}$ ,  $^{13}\text{CO}$ , and  $\text{C}^{18}\text{O}$ . The integrated line profiles were computed by integrating the emission in the regions corresponding to the dotted circles in Figure 2. The spectra may have been scaled for display purposes, as specified in each figure.

assuming two dust temperatures, 20 and 60 K. The former is the typical temperature of a passively heated protoplanetary disks (Williams & Cieza 2011), while the latter aims to represent more active, hotter, disks (see Takami et al. 2019). The derived disk dust masses are presented in Table 2. We also list the total disk mass (gas+dust) by assuming the standard gas-to-dust ratio of 100. The uncertainty for each variable parameter are estimated by considering the range around the median value that contains 68% of the walker positions (after removing the burn-in steps). The resulting channel maps for data, model, and residuals for  $^{13}\text{CO}$  and  $\text{C}^{18}\text{O}$  are shown in Figures A2 and A3, respectively.

FUor sources in our sample have masses of solids that are at least one order of magnitude larger than those of the EXors, consistent with the trend reported in Cieza et al. (2018). The assumed temperature plays a significant role. Adopting a three times higher disk temperature yields a reservoir of solids  $\sim 3.6$  times smaller in mass.

The dust mass estimate for UZ Tau E is consistent with the value derived by Long et al. (2018) using higher-resolution data at similar frequency ( $67 M_{\oplus}$  or  $2.2 \times 10^{-4} M_{\odot}$ ). Assuming a 100:1 gas-to-dust ratio, the total disk mass is  $2.2 \times 10^{-2} M_{\odot}$ . The total disk mass can also be obtained by comparing the  $^{13}\text{CO}(2-1)$  to  $\text{C}^{18}\text{O}(2-1)$  integrated line ratios to the grid of models from Williams & Best (2014). These models take into account basic CO chemistry (photodissociation and CO freeze-out) and provide an estimate of the total gas mass independent of the assumed gas-to-dust ratio. The comparison to the models yields a total gas mass of  $3.2 \times 10^{-3} M_{\odot}$ . Together with the dust mass estimated above, this implies a gas-to-dust ratio of 14, which is similar to the low ratios found around the EXor prototype EX Lupi and other Class II disks around Lupus (Ansdell et al. 2016; Miotello et al. 2017; Hales et al. 2018). This may be due to physically low amounts of gas, chemical conversion of CO into other species, or other physical processes (Bosman et al. 2018; Krijt et al. 2018; Schwarz et al. 2018).

We use radiative transfer codes in combination with Markov Chain Monte Carlo (MCMC) methods to infer the UZ Tau E disk parameters from the continuum and line data independently. The dust and gas disks are modeled separately using the radiative transfer code RADMC-3D (Dullemond et al. 2012), adopting the standard tapered-edge model to describe the surface density profiles. See Appendix A for details on the modeling and MCMC procedure. These methods provide an alternative estimation of the disk dust and gas masses. We find that the masses of the dust and gas disks are  $92.9^{+3.6}_{-13.3} M_{\oplus}$  ( $2.8 \times 10^{-4} M_{\odot}$ ) and  $7.8 \times 10^{-4} M_{\odot}$ , respectively.

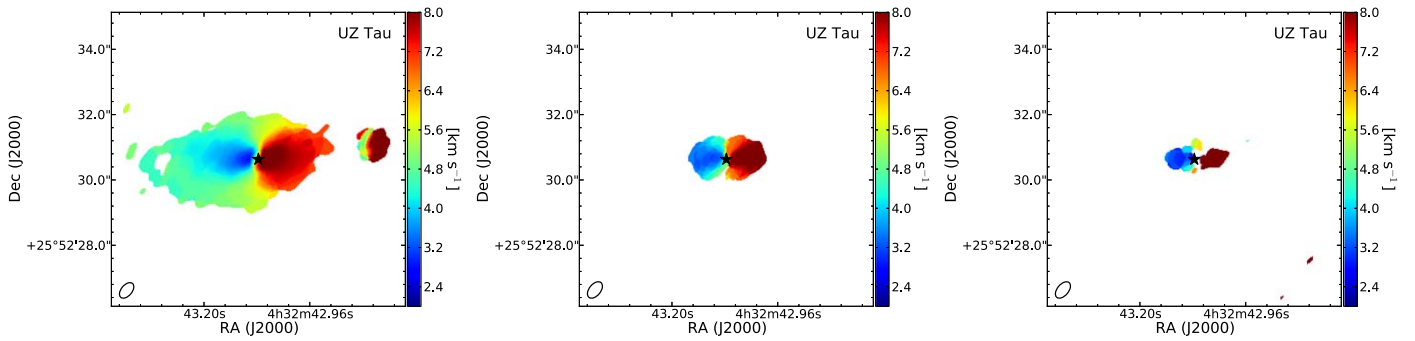
Both methods of deriving disk masses, from continuum and line emission, have caveats. The continuum radiative transfer modeling only accounts for a passive disk in hydrostatic equilibrium. While this is arguably a decent approximation of a protoplanetary disk, it may be far from the thermodynamical structure of actively accreting sources whose energy budget should include extra energy terms such as viscous heating, for example. This simplistic temperature structure also affects the molecular gas line modeling. The line modeling additionally suffers from uncertainties in CO isotopolog abundance ratios and a limited accounting of photodissociation and freeze-out of the CO molecules. Bearing these caveats in mind, it is still possible to use these masses to gain a rough idea of the gas-to-dust mass ratio. This ratio would be approximately 2.8 for UZ Tau E, suggesting its disk has a higher concentration of dust or a lower amount of gas, than the canonical assumption of a gas-to-dust mass of 100. The gas mass may have been reduced due to disk-binary interactions (see, for example, Czekala et al. 2019).

The total disk mass for V582 Aur, estimated assuming the dust emission, is optically thin ( $1055 M_{\oplus}$ ) and a gas-to-dust ratio of 100, is  $0.3 M_{\odot}$ , which is a factor of 7.5 larger than the estimate of Ábrahám et al. (2018). This discrepancy is mostly due to the new Gaia DR2 distance used in this work (2.5 kpc instead of 1.3 kpc) and cooler dust temperature (20 K instead of 30 K).

#### 4.2. Disk Sizes

Figure 6 shows an updated version of Figure 6 in Cieza et al. (2018), in which disk sizes and total disk masses from the FU/EXor sample are compared to those of other protostellar and protoplanetary sources observed by ALMA (Kóspál et al. 2017; Cieza et al. 2018; Hales et al. 2018; Kospal 2018; Cruz-Sáenz de Miera et al. 2019; Takami et al. 2019; Pérez et al. 2020, and also this work). The properties of Class 0 and I protostellar disk candidates in Orion (Tobin et al. 2020) and the Class II disks in Lupus (Ansdell et al. 2016) are shown for comparison. We also compare the properties of eruptive sources to those of protostellar and protoplanetary disks in Ophiuchus from the Ophiuchus DIsk Survey Employing ALMA (ODISEA; Cieza et al. 2019), which currently contains 12 Class I and 26 Class II sources with measured 1.3mm fluxes and resolved disk sizes.

The disk masses for the ODISEA sample are estimated assuming an optically thin dust continuum, a dust temperature of 20 K, and a gas-to-dust ratio of 100. Disk sizes are estimated from the deconvolved Gaussian FWHM/2 radius obtained from 2D Gaussian fits to the continuum images. Cieza et al. (2018) used the characteristic radius  $R_c$  (see Appendix A.1) as a



**Figure 4.** Maps of projected velocity centroids (moment 1) in  $^{12}\text{CO}$  (left),  $^{13}\text{CO}$  (middle), and  $\text{C}^{18}\text{O}$  (right) for UZ Tau E.

proxy for disk radius, while other authors have used the Gaussian  $2\sigma$  radius or the curve-of-growth method to estimate the radius that contains a certain fraction of the total disk mass (Bate 2018) or a fraction of the total flux (Tripathi et al. 2017; Ansdell et al. 2018; Trapman et al. 2019). There are advantages to and caveats on the ability of each method to measure the true sizes of circumstellar disks, which is beyond the purpose of this work (see discussions in e.g., Tripathi et al. 2017; Bate 2018; Tobin et al. 2020). We choose to use the deconvolved Gaussian FWHM/2 radius because it provides an homogeneous measure across the selected ALMA data sets.

We find that the new eruptive sources presented here follow the same trend as the sample in Cieza et al. (2018), in which FUor disks are more massive than Class II sources of similar size. In contrast, the properties of the EXor disks are more consistent with those of Class II objects. As noted by Tobin et al. (2020), there does not seem to be a clear distinction in disk sizes between Class II in Lupus and the younger Class 0/I in Orion. Interestingly, we also find no difference when comparing the Class II disk sizes to the Class I sources in Ophiuchus. This suggests that for a given disk size, the disks around FUor disks are brighter than disks of all protostellar classes. EXor disks, on the other hand, do not seem to be different from noneruptive disks.

Two FUor disks deviate from this trend, FU Ori North and L1551 IRS 5 North; both of them are binary systems. The class prototype FU Ori North hosts the smallest disk of all eruptive targets (Liu et al. 2019; Pérez et al. 2020), which is part of a 210 au separation binary system. Both disks in the FU Ori system have similar 1.3mm sizes. Cruz-Sáenz de Miera et al. (2019) detected compact disks of similar sizes in another binary FUor-like system L1551 IRS 5. Recently, A. Zurlo et al. (2020, in preparation) resolved for the first time two binary components and their respective disks in the HBC 494 system, which are also compact ( $<20$  au). The small disk sizes found around binary FUor systems are consistent with observations of noneruptive multiple systems in Orion. Tobin et al. (2020) found that multiple systems show the smallest (and faintest) distribution of disk sizes, which indicate that multiplicity has a significant impact on disk evolution. The disk sizes measured around binary FUor systems are consistent with simulations of stellar flybys in binary systems by Cuello et al. (2019). These simulations show that stellar encounters can deplete the disk outer regions and increase inner disk density, which can in turn enhance stellar accretion and explain the accretion outbursts of binary FUor systems.

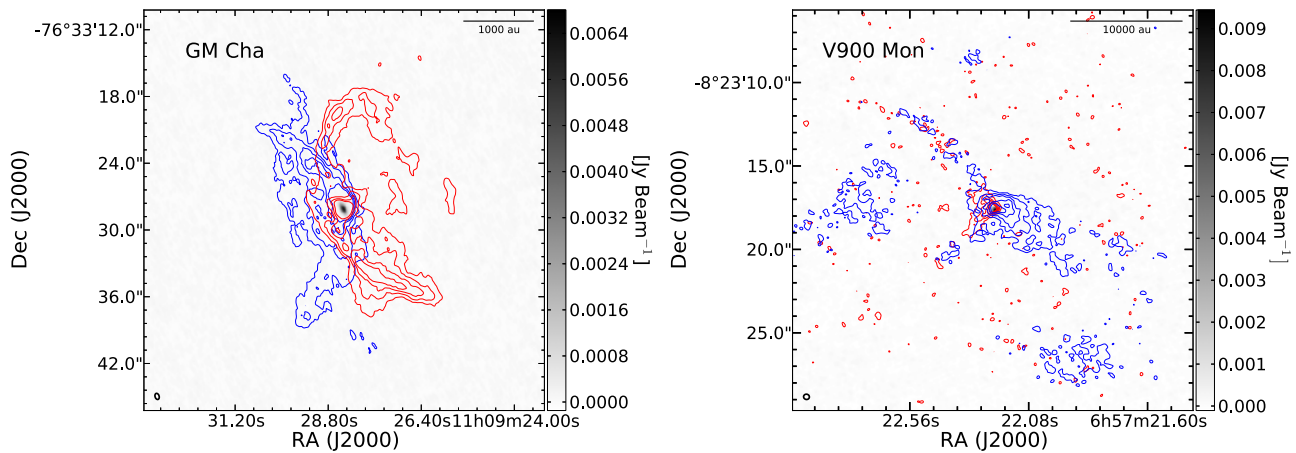
The power-law fits in Figure 6 can be inverted to estimate the relation of disk radius with disk mass. Tobin et al. (2020) report a power-law relation between disk radius and mass of  $R \propto M^{0.30 \pm 0.03}$ , which is similar to the power-law scaling

predicted by models of disk formation regulated by magnetic fields (which depend on magnetic field strength, ambipolar diffusion timescale, and combined disk+stellar mass). The power-law dependence for Class II in Lupus is steeper ( $R \propto M^{0.46 \pm 0.09}$ ), closer to the square-root dependence predicted for optically thick disks. The fit to the FUor sample indicates that disk radii increase with mass as  $R \propto M^{0.27 \pm 0.15}$ . This is closer to the value of 0.3 found for Class 0/I protostars in Orion although with a larger uncertainty dominated by low number statistics. Increasing the FUor sample observed at sufficient high angular resolution will help improve the accuracy of the fit and allow a more consistent comparison with larger samples of Class 0/I and Class II sources. The size–luminosity relation has been studied intensively around over 200 Class II disks, for which a correlation between millimeter luminosity and dust disk size of  $L \propto R^2$  has been well characterized (in agreement with the  $R \propto M^{0.46}$  found for the Class II in Lupus, because millimeter luminosity is a proxy for mass; Tripathi et al. 2017; Andrews et al. 2018). Rosotti et al. (2019) showed that the size–luminosity relation can be explained by grain growth and radial drift, although it could also be related to disk initial conditions or to optical depth effects (Andrews et al. 2010; Andrews 2020, and references therein). Measuring the size–luminosity relation in episodically accreting disks, which are thought to be a common early phase of the evolution of disks around low-mass stars, may inform on the initial unruly dynamics of protoplanetary disks. If these active disks indeed reveal an earlier stage in disk evolution, their size–luminosity relation allows for a more realistic description of the initial condition for later disk models, as an alternative for the classical “steady-state” start.

### 4.3. Gas Kinematics and Morphology

Complex kinematics can be the product of several types of dynamical interactions, such as flybys and binary interactions, outflows and winds, embedded planets and vortices, and the capture of cloud material. Several active sources are known binaries, such as UZ Tau E, for example, and recent hydrodynamic models of tidal interactions have shown that tidal encounters have distinct kinematics signatures (Cuello et al. 2019) and that these encounters may be related to outbursting events. Interactions with an embedded substellar perturber can excite kinematic perturbations (Pérez et al. 2015), which could persist on large scales in the disk (Pérez et al. 2018). On the other hand, Dullemond et al. (2019) recently speculated that outbursting systems may be the result of cloudlet capture events, which do bear observational kinematics in the form of complex tail-like features in maps of line emission.





**Figure 5.** Left: blue and red contours show the integrated intensity of the  $^{12}\text{CO}$  blue- and redshifted lobes of GM Cha (integrated between  $-10$  and  $4.5\text{ km s}^{-1}$  and  $6.5$  and  $14.5\text{ km s}^{-1}$  respectively). Contour levels start at  $3\sigma$ , increasing in steps of  $2\sigma$ . The  $1.3\text{mm}$  continuum image is shown in grayscale. Right: same for V900 Mon. Emission for the blue and red lobes was integrated between  $13.5$  and  $15.0\text{ km s}^{-1}$  and  $15.5$  and  $18.0\text{ km s}^{-1}$  respectively. Contour levels start at  $1.5\sigma$ , increasing in steps of  $2\sigma$ .

The molecular line data for the four sources observed have distinctive morphological features. GM Cha and V900 Mon  $^{12}\text{CO}(2-1)$  integrated maps show the presence of wide-angle conical cavities. The presence of an  $^{12}\text{CO}(3-2)$  outflow around GM Cha was first reported by Mottram et al. (2017) using APEX. The blueshifted and redshifted lobes are more clearly distinguished in GM Cha, while in V900 Mon the distinction is less clear. These morphologies are similar to the one observed in V883 Ori, HBC 494, V2775 Ori, and V1647 Ori (Ruíz-Rodríguez et al. 2017a, 2017b; Zurlo et al. 2017; Principe et al. 2018), in which opening cavities in  $^{12}\text{CO}(2-1)$  are reported around all FUor candidates but not around EXors. The observed emission is interpreted as the walls of a cavity that is carved out by a slow-moving outflow, probably produced by material swept up by a faster jet bow shock (Frank et al. 2014). As the sources evolve from Class I to Class II, outflows carve out cavities that widen as the source ages (Arce & Sargent 2006), in a process that results in the dispersion of the remaining prestellar core. Combining ages derived using the  $L_{\text{bol}}$ -age relation from Ladd et al. (1998) and the measured opening angles, Arce & Sargent (2006) found that sources with opening angles larger than  $\sim 150^\circ$  have ages of  $\sim 10^6$  yr, closer to the typical ages of Class II stars.

The opening angles for the blue- and redshifted lobes of GM Cha are both very similar,  $\sim 120^\circ$ , measured at a distance of  $1300\text{ au}$ . For V900 Mon, the opening angle measured on the blueshifted lobe is  $\sim 90^\circ$ . The opening angles of GM Cha are comparable to wide opening angles of  $150^\circ$  measured around HBC 494 and V883 Ori (Ruíz-Rodríguez et al. 2017a, 2017b). As noted by Takami et al. (2019), the opening angle of  $\sim 90^\circ$  around V900 Mon is narrower than the one around these sources, but wider than the one measured around the eruptive Class 0 protostar V346 Nor (Kóspál et al. 2017).

The presence of outflows in FUor sources (Kóspál et al. 2017; Ruíz-Rodríguez et al. 2017a, 2017b; Zurlo et al. 2017) and not around EXors suggests a distinction in the evolutionary stages between the two classes, with FUors closer to Class I sources. Nevertheless, EX Lupi and the ambiguously FUor/EXor classified V1647 Ori also have outflows (Hales et al. 2018; Principe et al. 2018). The outflows around these two EXors are fainter than the ones around FUors; therefore, the distinction is more subtle and supports the idea of a continuous

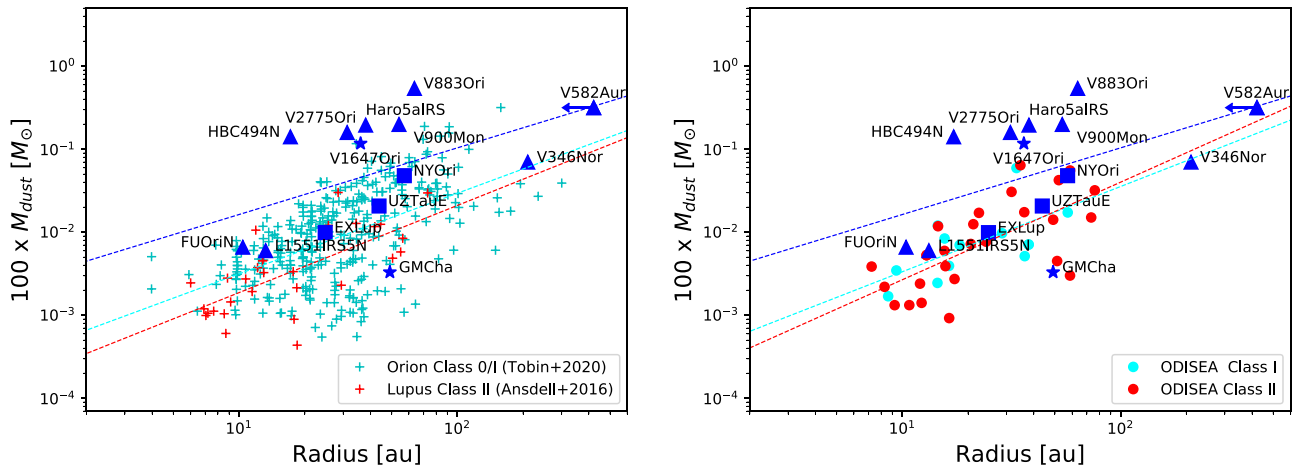
evolution from FUor to EXor, with EXors more evolved than FUors.

V582 Aur does not show a clear opening cavity but this may be due to the greater distance to the source. As a point of reference, V900 Mon is two times closer than V582 Aur but its outflow cavity walls were barely detected above the noise in our data. Another possibility is that the optical variability in V582 Aur is due to variable extinction and not accretion outbursts (Ábrahám et al. 2018). This would reinforce the picture that prominent cavity walls are carved during strong accretion outbursts. Deeper, higher-resolution images of the more compact emission observed at the V582 Aur position could provide better understanding of its kinematics and relation to the FUor.

UZ Tau E, the only bona fide EXor from our sample, is noticeably different from the FUors. It shows the clear Keplerian pattern of a Class II disk. This supports the evolutionary distinction between EXors and FUors. Cloud or envelope emission is most likely responsible for why Keplerian rotation is difficult to observe around most FUors.  $^{12}\text{CO}$  and  $^{13}\text{CO}$  are typically too contaminated by envelope emission, but a Keplerian disk is clearly seen in  $\text{C}^{18}\text{O}$  in V883 Ori (Cieza et al. 2016). It is possible that Keplerian rotation is not detected in some FUors simply because the observations are not deep enough, as  $\text{C}^{18}\text{O}$  is generally too faint for easy detection in other lower-mass stars (Ansdell et al. 2018). Ansdell et al. (2018) detected  $\text{C}^{18}\text{O}$  in the most massive disks in their sample; however, most FUors are located two to three times farther away than Lupus, with more extreme cases such as V900 Mon and V582 Aur that are 10 and 15 times more distant than Lupus, respectively). Another possibility is that FUor disks are too perturbed and their kinematics distorted (due to the potential disk precession; Principe et al. 2018). High-resolution observations of FU Ori reveal a rotation pattern distorted by complex kinematics (Pérez et al. 2020) possibly tracing binary interactions near the base of the outflow.

#### 4.4. Triggering Mechanisms

Observations of FUor objects suggest that the FUor phenomenon is a heterogeneous process. Some systems harbor large, massive disks such as the ones detected around V883 Ori, V2775 Ori, and V582 Aur. High-resolution millimeter observations have also identified binary systems with



**Figure 6.** Relationship between disk mass and disk radius (FWHM/2) for FUor/EXor sources presented here (assuming a 20 K dust temperature) and in the literature. Squares are EXors, triangles are FUors, and objects with double FUor and EXor classification are marked with a star symbol. The disk size and mass for HBC 494 correspond to the ones measured toward the brightest component of the binary, HBC 494 North (A. Zurlo et al. 2020, in preparation). The horizontal arrow on V582 Aur denotes the disk radius is an upper limit. Left panel: light blue crosses show the disk masses and radii (FWHM/2) for Class 0 and I protostellar disk candidates in Orion derived from 0.87 mm ALMA observations (Tobin et al. 2020). Red crosses show the disk masses and disk radii for Class II sources in Lupus from Ansdell et al. (2016). The dashed lines correspond to power-law fits to the Class 0/I, Class II, and FU/EXor data, respectively. Right panel: same as left panel, but now comparing the FU/EXor data to Class I and Class II sources in Ophiuchus from the ODISEA sample (Cieza et al. 2019).

compact, hot disks in each of the components (like FU Ori itself, HBC 494, and L1551 IRS 5).

Gravitational instability requires that the mass of the disk is at least 10% of the mass of the central star in order to operate (see discussion in Cieza et al. 2018 and references therein) and could possibly explain the outburst in the most massive disks. However, high-resolution observations do not show the signatures predicted by theoretical simulations of gravitationally unstable disks, as was demonstrated in the case of V883 Ori. High-resolution ALMA images did not reveal the spiral or clumpy features predicted by gravitational instability simulations (Cieza et al. 2016). V582 Aur hosts the most massive disk in our sample, yet being located 2.5 kpc away, it was unresolved by our observations, and therefore, we are unable to test the gravitational instability scenario. Nevertheless, none of the massive FUor disks that have been resolved so far have shown these signatures, which at least rules out the possibility of gravitational instability operating in spatial scales compared to the spatial resolution of the observations. As pointed out by Cieza et al. (2018), the lack of large-scale instabilities of fragmentation in these observations suggest that the outburst of these systems could support models that combine MRI and gravitational instability without fragmentation (e.g., Zhu et al. 2009).

The outbursts in binary systems could be explained by the perturbation of the accretion disk by a stellar companion. Bonnell & Bastien (1992) showed that binary perturbation can render the disk unstable and could possibly explain the triggering of FUor outbursts in multiple systems. As mentioned earlier, a stellar flyby scenario could also explain the compact sizes of the disks in binary systems as simulations by Cuello et al. (2019) show that an inclined prograde encounter can remove material from the outer disk and increase the inner disk density (which in turn can enhance the accretion).

Observations of EXors reveal disks that are similar to those observed around typical Class II sources, both in size and mass. The disks are not massive enough to satisfy the requirement for triggering gravitational instability. Most EXors resolved by ALMA so far, with the exception of UZ Tau E, are single-star

systems and therefore there is no clear connection between the EXor phenomenon and stellar multiplicity. As pointed out already by Cieza et al. (2018), the triggering mechanisms for the EXor outburst are more likely associated with instabilities in the inner disks and/or interactions between the disk and planetary companions (Lodato & Clarke 2004).

## 5. Conclusion

We conducted a campaign to observe four young eruptive stellar systems with ALMA at 0".4 resolution. This sample represents 10% of known FUor/EXor objects in the non-exhaustive list of eruptive young stars from Audard et al. (2014), increasing the number of eruptive sources observed at subarcsecond resolution by 15%. We detected 1.3mm continuum emission in all four sources.

We found that the FUors have dust disks that are more massive than those found around Class 0/I sources and Class II objects of similar size, making them more likely to become gravitationally unstable and trigger the outburst. The EXor in our sample has a dust and gas disk that is well modeled with a passively irradiated disk in hydrostatic equilibrium, similar to those found in Class II sources.

We find that two of the three FUor objects show prominent outflows in molecular gas emission. While the FUor V900 Mon shows a distinct conical cavity similar to those of Class I objects, the source with unclear FU/EXor classification (GM Cha) has a wide-angle outflow similar to those found around a subset of FUor objects such as V883 Ori and HBC 494 (and FU Orionis itself; A. S. Hales et al. 2020, in preparation). Although the sample size remains small, the presence of outflow activity in FUors but not in EXors suggests that the two types of objects represent different evolutionary stages, with EXors more evolved than FUors.

These results highlight the importance of spectral line observations sensitive to various spatial scales for inferring the nature of eruptive sources, which seem to span from Class 0 to the early Class II stages of protostellar evolution. Observations targeting larger-scale structure ( $>1000$  au) are required to

determine the properties of outflows around FUors (and confirm their absence in EXors), while deeper continuum and C<sup>18</sup>O observations at few astronomical unit resolution will measure the properties of their inner disks and help us understand what drives this important early phase of star formation.

We thank the anonymous referee for a very constructive report. S.P. acknowledges support from ANID-FONDECYT grant 1191934 and from the Joint Committee of ESO and the Government of Chile. A.Z. acknowledges support from the FONDECYT Iniciación en investigación project number 11190837. This paper makes use of the following ALMA data: ADS/JAO.ALMA#2017.1.01031.S. ALMA is a partnership of ESO (representing its member states), NSF (USA) and NINS (Japan), together with NRC (Canada) and NSC and ASIAA (Taiwan), in cooperation with the Republic of Chile. The Joint ALMA Observatory is operated by ESO, AUI/NRAO, and NAOJ. The National Radio Astronomy Observatory is a facility of the National Science Foundation operated under cooperative

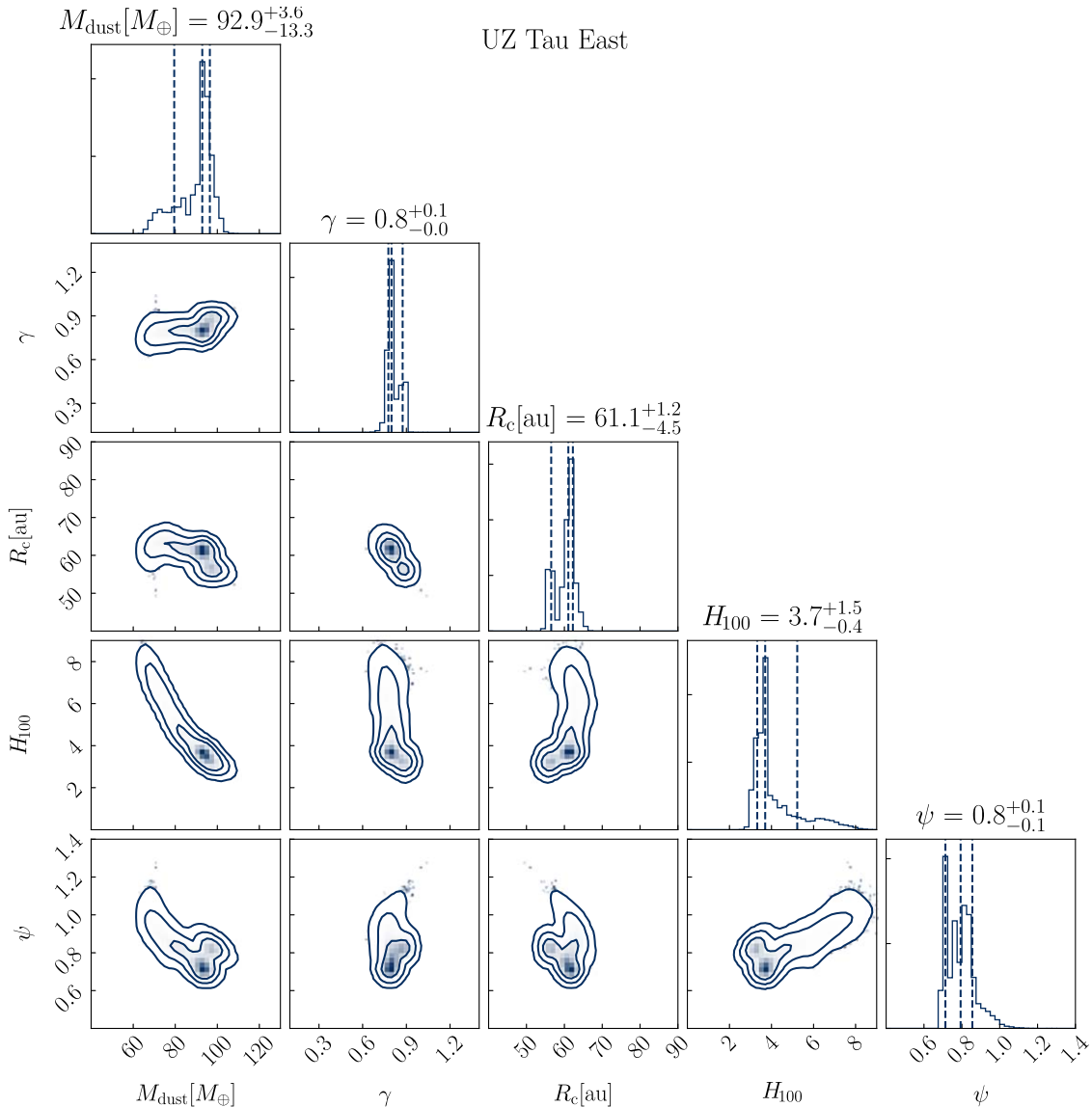
agreement by Associated Universities, Inc. This work has made use of data from the European Space Agency (ESA) mission Gaia (<https://www.cosmos.esa.int/gaia>), processed by the Gaia Data Processing and Analysis Consortium (DPAC, <https://www.cosmos.esa.int/web/gaia/dpac/consortium>). Funding for the DPAC has been provided by national institutions, in particular the institutions participating in the Gaia Multilateral Agreement.

*Software:* Common Astronomy Software Applications (McMullin et al. 2007), RADMC-3D, (Dullemond et al. 2012), GALARIO, (Tazzari et al. 2017, 2018), EMCEE (Foreman-Mackey et al. 2013), Astropy (Astropy Collaboration et al. 2013).

## Appendix A Radiative Transfer Modeling of UZ Tau E

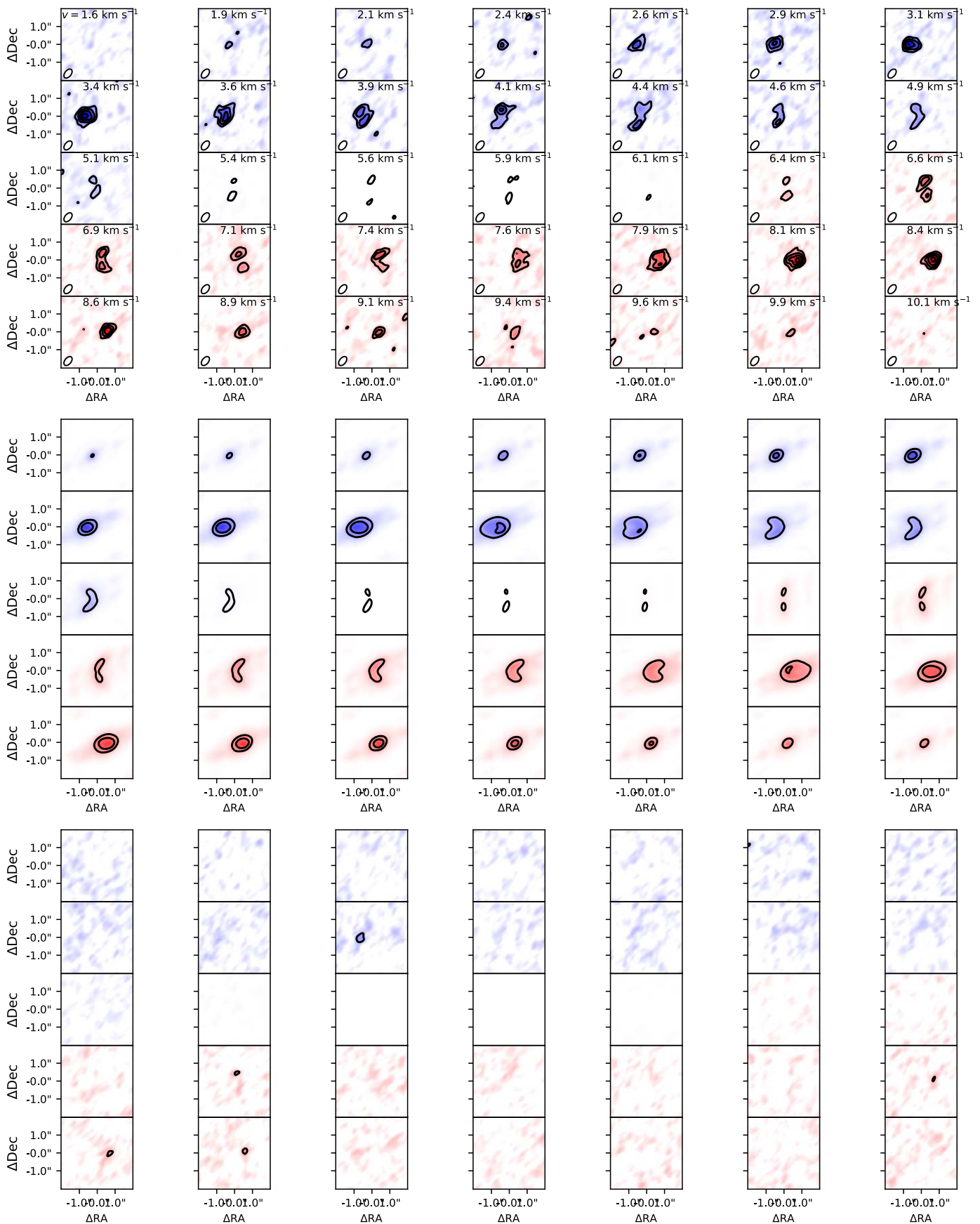
### A.1. Dust Continuum Model

The millimeter continuum disk around UZ Tau E has been studied intensively in previous works: Tripathi et al. (2018) using CARMA, Long et al. (2018) and Manara et al. (2019)



**Figure A1.** Triangle plots of the posterior probability distribution function for the different model parameters.





**Figure A2.**  $^{13}\text{CO}$  channel maps for UZ Tau E (top), best-fit disk model (middle), and residuals (bottom). Contour levels start at  $3.5\sigma$ , with increments of  $3\sigma$ .

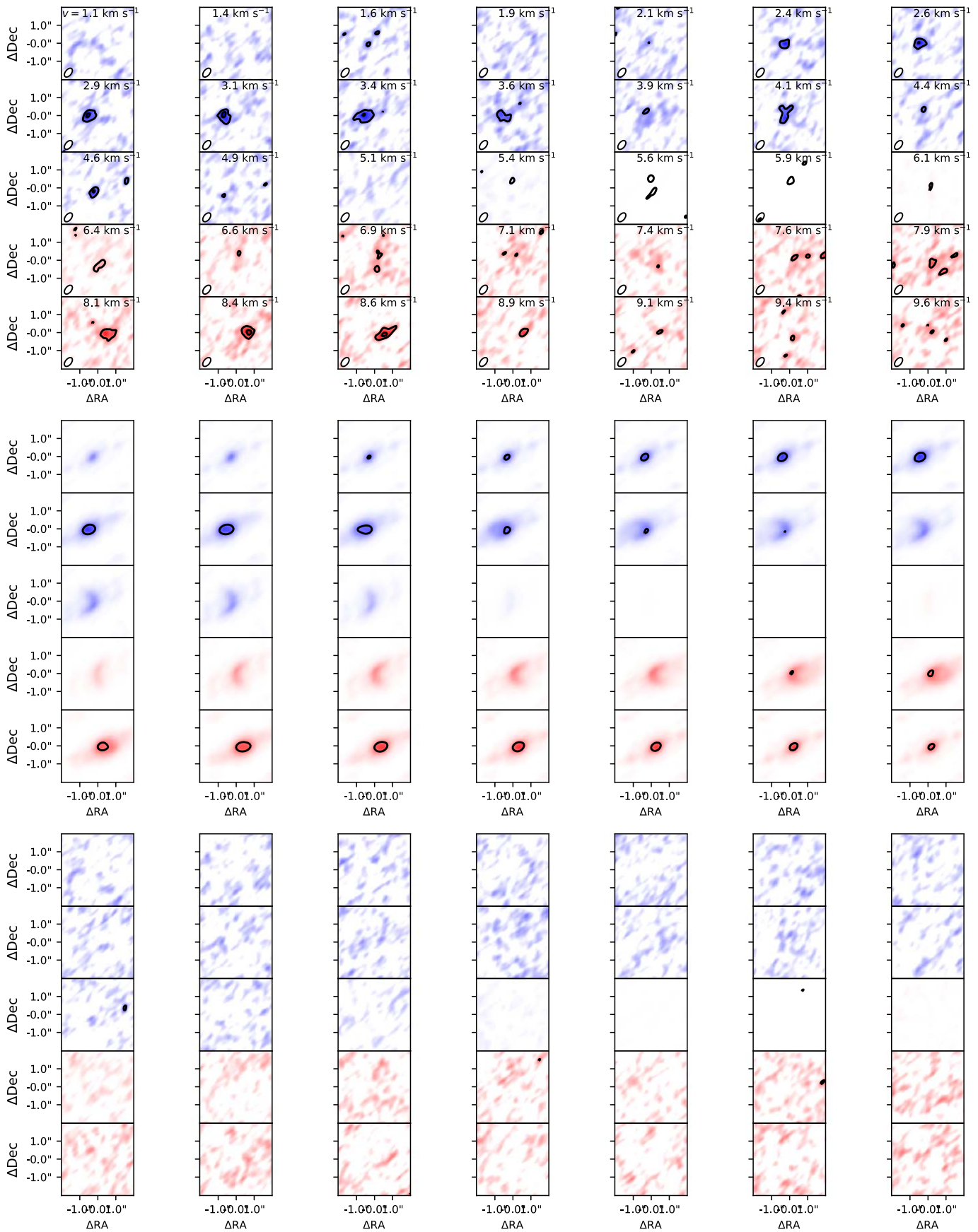


Figure A3.  $C^{18}O$  channel maps for UZ Tau E (top), best-fit disk model (middle), and residuals (bottom).

using higher-resolution ALMA data. To compare the properties (mainly size and perhaps the mass) of the dust disk around UZ Tau E to the ones of other eruptive sources studied by our group, we modeled the continuum emission with a simple passively heated disk. The model assumes a power law for the surface density profile with an exponential taper beyond a characteristic radius. The exact formulation of the model and the radiative transfer calculation are described in Cieza et al. (2018), Hales et al. (2018), and Pérez et al. (2020)—we refer the readers to these works for a detailed description of the radiative transfer modeling.

The disk model is described by five free parameters: the dust mass  $M_{\text{disk}}$ , the slope of the surface density power law  $\gamma$ , the characteristic radius  $R_c$ , the scale height at 100 au  $H_{100}$ , and the flaring index  $\Psi$ . The flux emerging from the parametric disk model is computed using the radiative transfer code RADMC-3D (version 0.41; Dullemond et al. 2012).

The stellar parameters that we adopt for UZ Tau E are an effective stellar temperature of 3574 K and a luminosity of  $0.35 L_{\odot}$  (Long et al. 2018). The assumed distribution of dust grains and their optical properties are the same as the ones adopted in our previous works (the dust absorption opacity at 1.3 mm is  $\kappa_{\text{abs}} = 0.022 \text{ cm}^2 \text{ g}^{-1}$ ). The inclination angle  $i$  and position angle (PA) of the model are fixed to the values derived by Long et al. (2018) from higher-resolution images.

The EMCEE MCMC algorithm (Foreman-Mackey et al. 2013) was used to sample the posterior distributions of each parameter. We run radiative transfer models with 240 walkers for 1000 iterations. The resulting posteriors are shown in Figure A1. We note that as the model is a passive disk (it ignores, for example, viscous heating), the derived temperatures serve only as a crude approximation for the dust temperature. Nevertheless, the best-fit (maximum likelihood set of parameters) model allows a crude estimate of the size and bulk mass of the disk to be obtained. The 1.3 mm observations of UZ Tau E can thus be described by a disk profile with characteristic radii of 61 au and total dust mass of  $92.9 M_{\oplus}$  ( $2.8 \times 10^{-4} M_{\odot}$ ). The slope of the surface density distribution is 0.8, similar to those of T Tauri stars (Andrews et al. 2010). See Figure A1 for parameter uncertainties. The parameters' posterior distributions show that there could be some degeneracies in our modeling. We think this is could be due to underlying structures not accounted for in our simple model. Higher-resolution data, and a more complete model that includes viscous heating, would be required to describe the UZ Tau E disk in detail.

## Appendix B $^{13}\text{CO}$ and $\text{C}^{18}\text{O}$ Gas Model

In this section, we focus on modeling of the  $^{13}\text{CO}$  and  $\text{C}^{18}\text{O}$  gas emission detected by our ALMA observations. We use the PDSKY code from Sheehan et al. (2019) to generate synthetic molecular line emission channel maps from a model of a Keplerian-rotating, passively irradiated disk in hydrostatic

equilibrium. The models are then used to fit the  $^{13}\text{CO}$  and  $\text{C}^{18}\text{O}$  data simultaneously using an MCMC routine. The code is described in detail in Sheehan et al. (2019), and it uses RADMC-3D to ray-trace the density and temperature structure, and GALARIO for fast sampling of the visibilities from the synthetic channel maps generated by RADMC-3D (Tazzari et al. 2018). The model visibilities are then provided as input to an MCMC routine that makes use of the EMCEE code (Foreman-Mackey et al. 2013) to compare the synthetic observations with our data.

The model adopted here includes 13 parameters: total disk mass  $M_{\text{disk}}$ , combined stellar mass  $M_*$ , disk characteristic radius  $R_{\text{disk}}$ , disk inner radius  $R_{\text{in}}$ ,  $T_0$ ,  $a_{\text{turb}}$ , PA,  $q$ , system velocity  $v_{\text{sys}}$  (LSRK), and offset from the phase center  $x_0$  and  $y_0$ . The dynamical mass of the central object  $M_*$  is fitted as part of our model, assuming the distance of  $131.2 \pm 1.7$  pc (Gaia Collaboration et al. 2018). The disk is assumed to be vertically isothermal, with a power-law radial dependence of the temperature given by

$$T(r) = T_0 \left( \frac{r}{1 \text{ au}} \right)^{-q}, \quad (\text{B1})$$

where  $T_0$  corresponds to the temperature at 1 au and  $q$  is the radial exponent for the temperature dependence. The surface density profile of the disk is given by Equation 1 in Sheehan (2019), with the vertical structure determined by hydrostatic equilibrium. Following Czekala et al. (2019), we fixed  $q$  to 0.5, the surface density power-law exponent  $\gamma$  to 1.0, and the inclination angle of the disk to  $56^{\circ}.16$ .  $M_{\text{disk}}$  is the total gas mass. The abundance of  $^{12}\text{CO}$  relative to  $\text{H}_2$  was set to  $10^{-4}$  and assumed constant throughout the disk. We adopt the canonical values for the  $^{13}\text{CO}$  and  $\text{C}^{18}\text{O}$  isotopolog ratios with respect to  $^{12}\text{CO}$  (77 and 550, respectively; Wilson & Rood 1994).

Each run was started with 100 walkers and were run for  $\sim 2500$  steps. Detailed description of the MCMC fitting procedure can be found in Appendix A1 of Sheehan et al. (2019). In Table B1 we show the best-fit parameters obtained by computing the median value of the MCMC samples after removing the burn-in steps. The triangle plots of the posterior probability distribution function from the MCMC fitting process are shown in Figure B1. The uncertainty for each variable parameter is estimated by considering the range around the median value that contains 68% of the walker positions (after removing the burn-in steps).

We find that a combined stellar mass for M1+M2 of  $1.25 \pm 0.009 M_{\odot}$  comparable to the  $1.3 \pm 0.08 M_{\odot}$  derived using  $^{12}\text{CO}$  from the IRAM Plateau de Bure interferometer (Simon et al. 2000) and to the  $1.23 \pm 0.12 M_{\odot}$  derived by Czekala et al. (2019) using ALMA data at  $0''.6\text{--}0''.7$  resolution of the same CO isotopologs in our data. We derive a total disk mass of  $0.00078 \pm 0.00003 M_{\odot}$ .

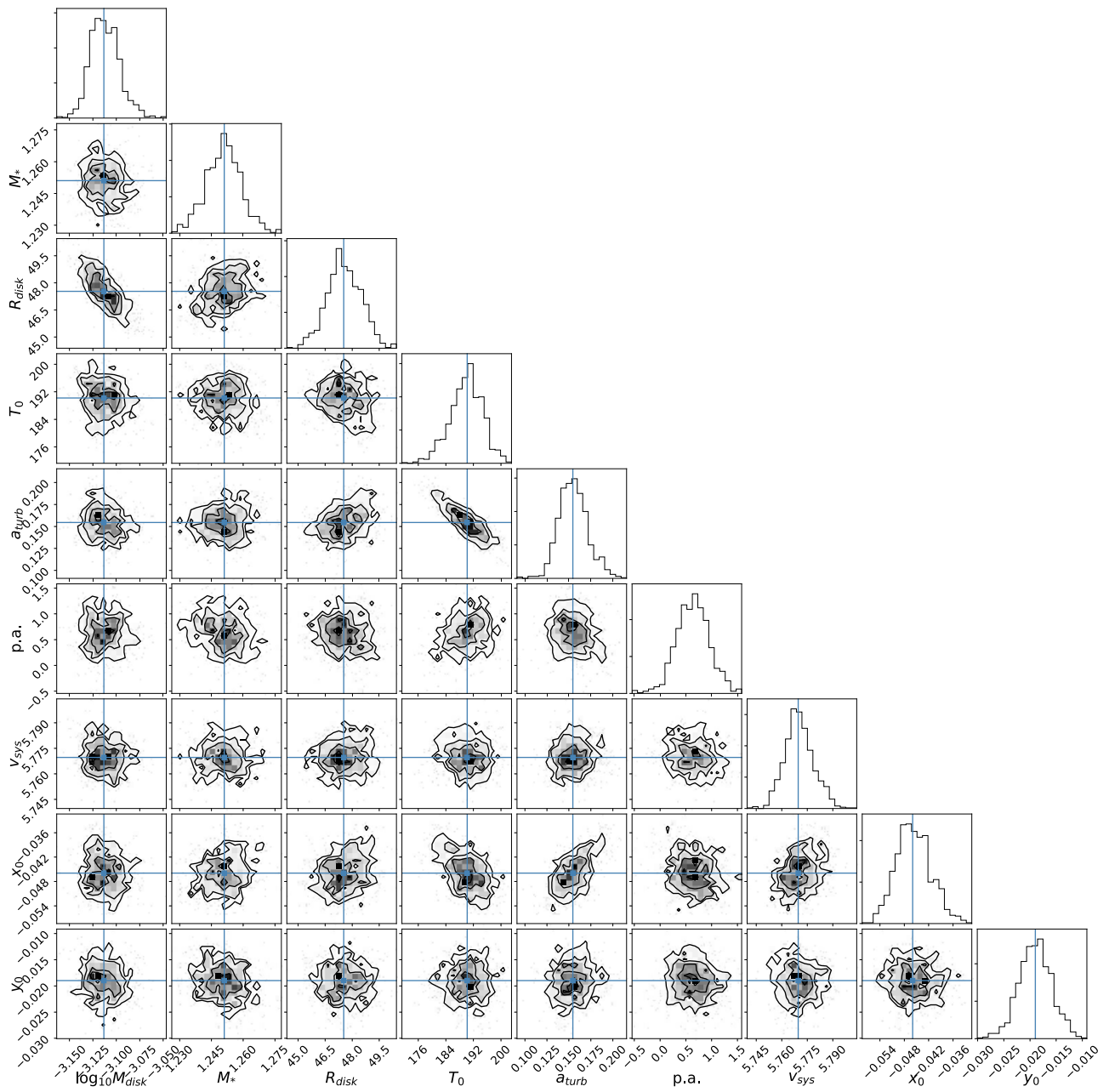


**Table B1**  
Best-fit Model Parameters for UZ Tau E

$\gamma$	$i$ ( $^{\circ}$ )	$M_{\text{disk}}$ ( $M_{\odot}$ )	$M_{*}$ ( $M_{\odot}$ )	$R_{\text{disk}}$ (au)	$R_{\text{in}}$ (au)	$T_0$ (K)	$a_{\text{turb}}$ ( $\text{km s}^{-1}$ )	pa ( $^{\circ}$ )	$q$	$v_{\text{sys}}$ ( $\text{km s}^{-1}$ )	$x_0$ (mas)	$y_0$ (mas)
1.0 <sup>a</sup>	56.15 <sup>a</sup>	$0.00078 \pm 0.00003$	$1.253 \pm 0.009$	$48.1 \pm 1.1$	1.0 <sup>a</sup>	$187.3 \pm 4.6$	$0.171 \pm 0.016$	$1.1 \pm 0.3$	0.5 <sup>a</sup>	$5.77 \pm 0.01$	$-0.051 \pm 0.004$	$-0.013 \pm 0.003$

**Note.**

<sup>a</sup> Parameter is fixed.

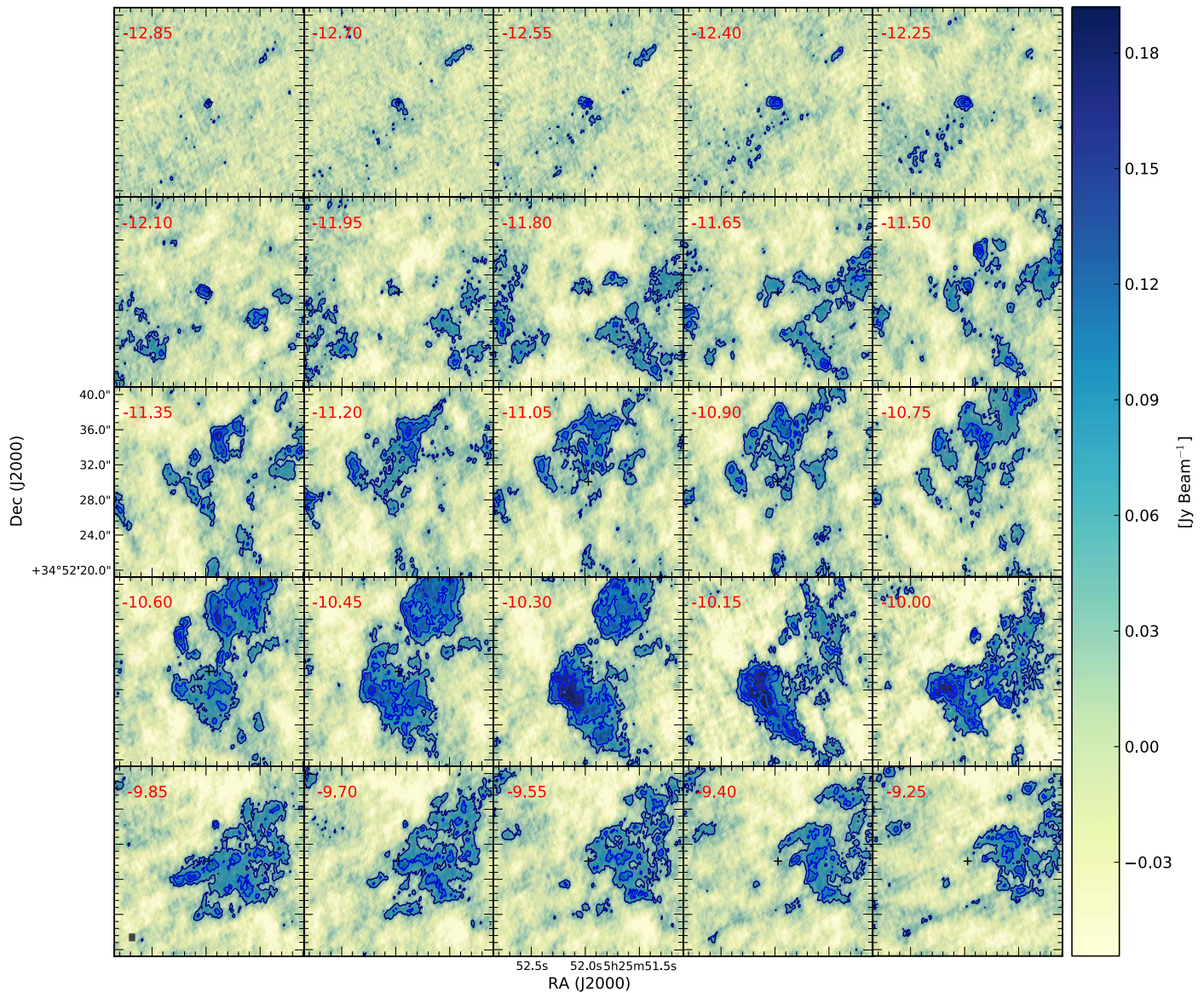


**Figure B1.** Triangle plots of the posterior probability distribution function for the different model parameters.

### Appendix C Channel Maps

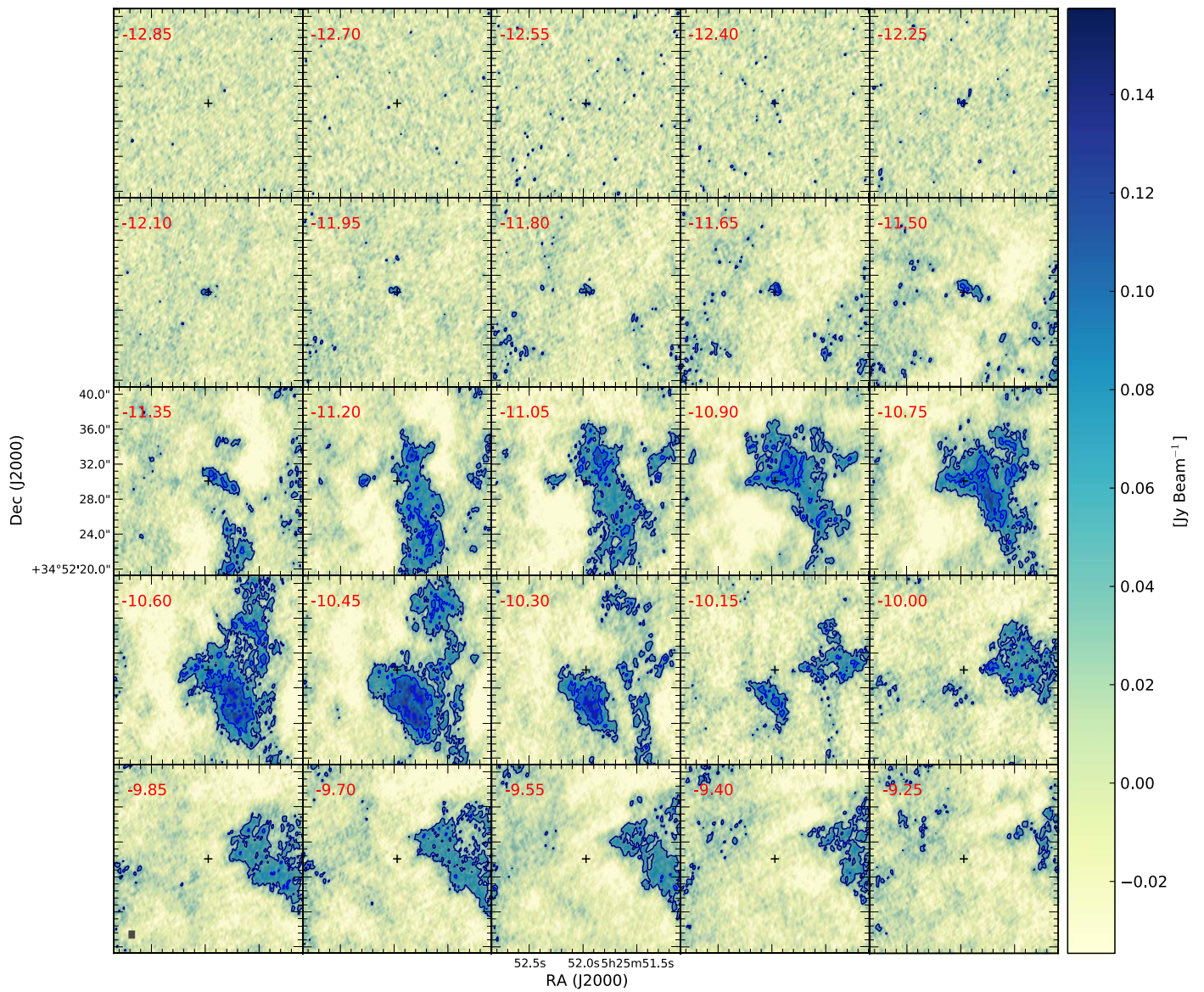
Figures C1–C3 show the channel maps for V582 Aur in  $^{12}\text{CO}(2-1)$ ,  $^{13}\text{CO}(2-1)$ , and  $\text{C}^{18}\text{O}(2-1)$ , respectively. Figure C4

shows the moment 0 maps for  $^{13}\text{CO}(2-1)$  and  $\text{C}^{18}\text{O}(2-1)$  computed in the same velocity ranges as Figure 2.



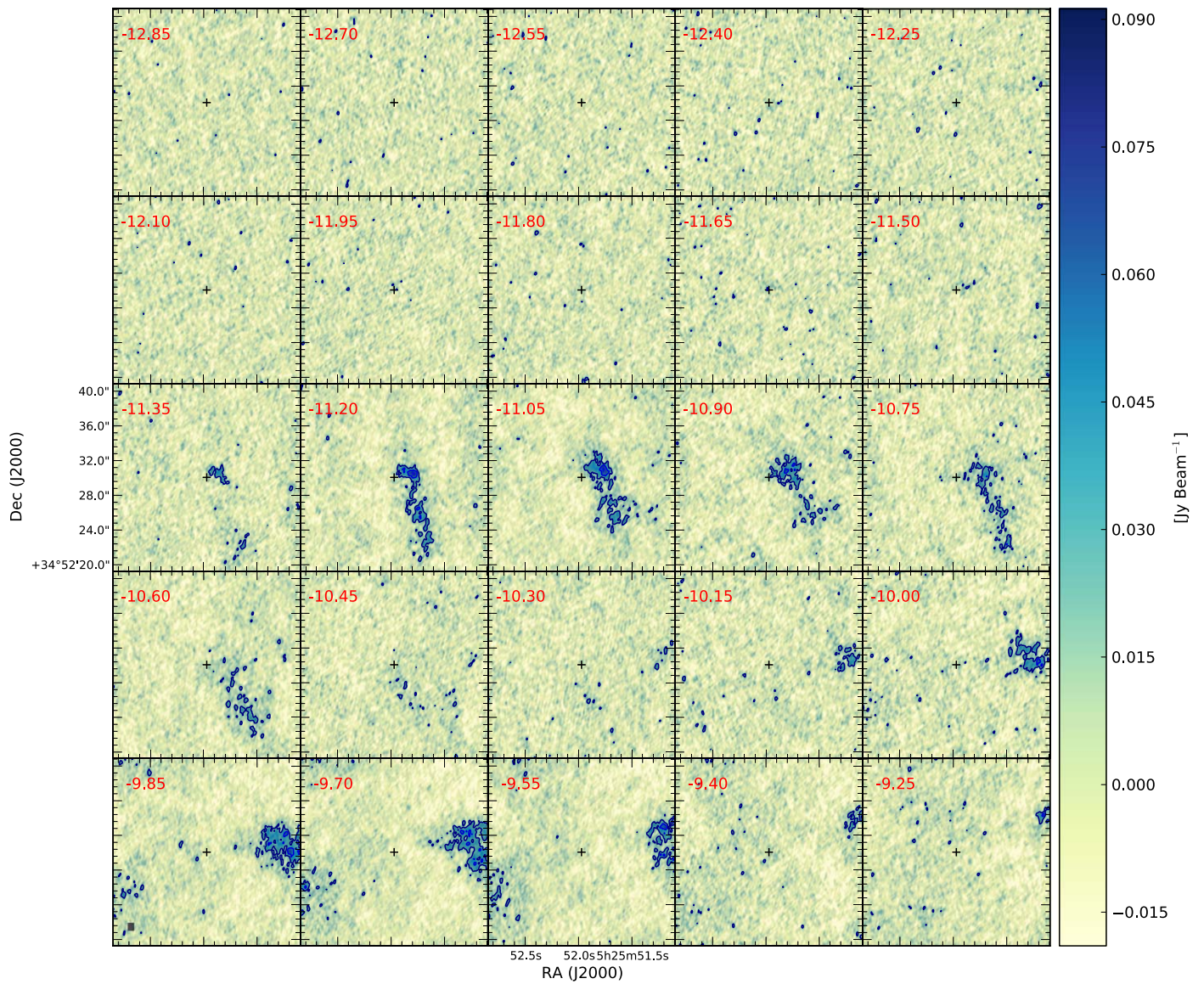
**Figure C1.**  $^{12}\text{CO}$  channel maps for V582 Aur. Contour levels start at  $3\sigma$ , increasing in steps of  $3\sigma$  ( $\sigma = 16 \text{ mJy beam}^{-1}$ ). The position of the star is marked with a cross. The beam is represented by a gray ellipse in the bottom-left corner of the bottom-left panel.



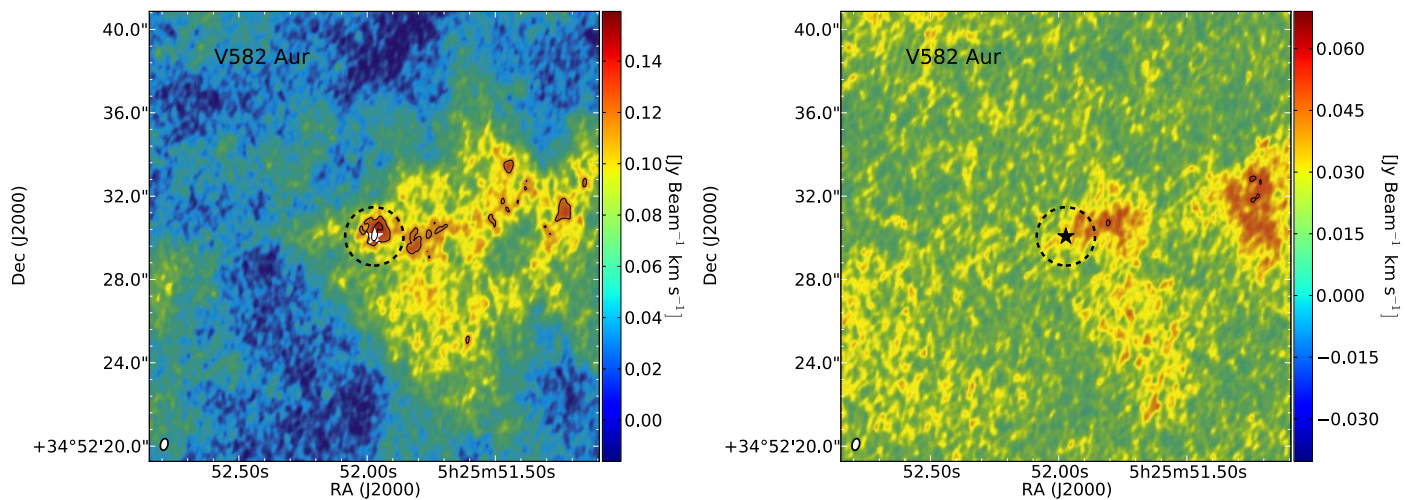


**Figure C2.**  $^{13}\text{CO}$  channel maps for V582 Aur. Contour levels start at  $3\sigma$ , increasing in steps of  $3\sigma$  ( $\sigma = 17 \text{ mJy beam}^{-1}$ ). The position of the star is marked with a cross. The beam is represented by a gray ellipse in the bottom-left corner of the bottom-left panel.





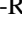

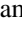






**Figure C3.**  $\text{C}^{18}\text{O}$  channel maps for V582 Aur. Contour levels start at  $3\sigma$ , increasing in steps of  $3\sigma$  ( $\sigma = 10 \text{ mJy beam}^{-1}$ ). The position of the star is marked with a cross. The beam is represented by a gray ellipse in the bottom-left corner of the bottom-left panel.



**Figure C4.**  $^{13}\text{CO}(2-1)$  and  $\text{C}^{18}\text{O}(2-1)$  moment 0 maps for V582 Aur (left and right panels, respectively). Contour levels start at  $3\sigma$ , increasing in steps of  $1\sigma$ . The dashed circles show the region used to compute the integrated line emissions listed in Table 3. The peak position of the continuum is shown with a star symbol. The moment 0 maps were computed in the same velocity ranges as Figure 2.

## ORCID iDs

Antonio S. Hales  <https://orcid.org/0000-0001-5073-2849>  
 Sebastián Pérez  <https://orcid.org/0000-0003-2953-755X>  
 Camilo Gonzalez-Ruilova  <https://orcid.org/0000-0003-4907-189X>  
 Lucas A. Cieza  <https://orcid.org/0000-0002-2828-1153>  
 Jonathan P. Williams  <https://orcid.org/0000-0001-5058-695X>  
 Patrick D. Sheehan  <https://orcid.org/0000-0002-9209-8708>  
 Simon Casassus  <https://orcid.org/0000-0002-0433-9840>  
 David A. Principe  <https://orcid.org/0000-0002-7939-377X>  
 Alice Zurlo  <https://orcid.org/0000-0002-5903-8316>

## References

- Ábrahám, P., Kóspál, Á., Kun, M., et al. 2018, *ApJ*, **853**, 28  
 Andrews, S. M. 2020, arXiv:2001.05007  
 Andrews, S. M., Terrell, M., Tripathi, A., et al. 2018, *ApJ*, **865**, 157  
 Andrews, S. M., Wilner, D. J., Hughes, A. M., Qi, C., & Dullemond, C. P. 2010, *ApJ*, **723**, 1241  
 Ansdell, M., Williams, J. P., Trapman, L., et al. 2018, *ApJ*, **859**, 21  
 Ansdell, M., Williams, J. P., van der Marel, N., et al. 2016, *ApJ*, **828**, 46  
 Arce, H. G., & Sargent, A. I. 2006, *ApJ*, **646**, 1070  
 Armitage, P. J., Livio, M., & Pringle, J. E. 2001, *MNRAS*, **324**, 705  
 Astropy Collaboration, Robitaille, T. P., Tollerud, E. J., et al. 2013, *A&A*, **558**, AA33  
 Audard, M., Ábrahám, P., Dunham, M. M., et al. 2014, in *Protostars and Planets VI*, ed. H. Beuther et al. (Tucson, AZ: Univ. Arizona Press), 387  
 Bate, M. R. 2018, *MNRAS*, **475**, 5618  
 Beckwith, S. V. W., Sargent, A. I., Chini, R. S., & Guesten, R. 1990, *AJ*, **99**, 924  
 Bonnell, I., & Bastien, P. 1992, *ApJL*, **401**, L31  
 Bosman, A. D., Walsh, C., & van Dishoeck, E. F. 2018, *A&A*, **618**, A182  
 Calvet, N., Hartmann, L., & Kenyon, S. J. 1993, *ApJ*, **402**, 623  
 Chiang, E. I., & Goldreich, P. 1997, *ApJ*, **490**, 368  
 Cieza, L. A., Casassus, S., Tobin, J., et al. 2016, *Natur*, **535**, 258  
 Cieza, L. A., Ruíz-Rodríguez, D., Hales, A., et al. 2019, *MNRAS*, **482**, 698  
 Cieza, L. A., Ruíz-Rodríguez, D., Pérez, S., et al. 2018, *MNRAS*, **474**, 4347  
 Connelley, M. S., & Reipurth, B. 2018, *ApJ*, **861**, 145  
 Cruz-Sáenz de Miera, F., Kóspál, Á., Ábrahám, P., et al. 2019, arXiv:1908.04649  
 Cuello, N., Dipierro, G., Mentiplay, D., et al. 2019, *MNRAS*, **483**, 4114  
 Czekala, I., Chiang, E., Andrews, S. M., et al. 2019, *ApJ*, **883**, 22  
 Dewangan, L. K., Baug, T., Ojha, D. K., et al. 2018, *ApJ*, **864**, 54  
 Dullemond, C. P., Juhasz, A., Pohl, A., et al. 2012, RADMC-3D: A Multi-purpose Radiative Transfer Tool, v.0.41, Astrophysics Source Code Library, ascl:1202.015  
 Dullemond, C. P., Küffmeier, M., Goicovic, F., et al. 2019, *A&A*, **628**, A20  
 Dzib, S. A., Loinard, L., Ortiz-León, G. N., et al. 2018, *ApJ*, **867**, 151  
 Evans, N. J., II, Dunham, M. M., Jørgensen, J. K., et al. 2009, *ApJS*, **181**, 321  
 Foreman-Mackey, D., Hogg, D. W., Lang, D., & Goodman, J. 2013, *PASP*, **125**, 306  
 Frank, A., Ray, T. P., Cabrit, S., et al. 2014, in *Protostars and Planets VI*, ed. H. Beuther et al. (Tucson, AZ: Univ. Arizona Press), 451  
 Gaia Collaboration, Brown, A. G. A., Vallenari, A., et al. 2018, *A&A*, **616**, A1  
 Grinin, V. P., Semenov, A. O., Barsunova, O. Y., et al. 2019, *Ap*, **62**, 41  
 Hales, A. S., Corder, S. A., Dent, W. R. D., et al. 2015, *ApJ*, **812**, 134  
 Hales, A. S., Pérez, S., Saito, M., et al. 2018, *ApJ*, **859**, 111  
 Hartmann, L. 2008, *Accretion Processes in Star Formation* (Cambridge: Cambridge Univ. Press)  
 Hartmann, L., Herczeg, G., & Calvet, N. 2016, *ARA&A*, **54**, 135  
 Hartmann, L., & Kenyon, S. J. 1985, *ApJ*, **299**, 462  
 Hartmann, L., & Kenyon, S. J. 1996, *ARA&A*, **34**, 207  
 Herbig, G. H. 1966, *VA*, **8**, 109  
 Herbig, G. H., & Harlan, E. A. 1971, *IBVS*, **543**, 1  
 Hildebrand, R. H. 1983, *QJRAS*, **24**, 267  
 Jensen, E. L. N., Dhital, S., Stassun, K. G., et al. 2007, *AJ*, **134**, 241  
 Johnstone, D., Herczeg, G. J., Mairs, S., et al. 2018, *ApJ*, **854**, 31  
 Jones, T. J., Hyland, A. R., Harvey, P. M., et al. 1985, *AJ*, **90**, 1191  
 Kenyon, S. J., Hartmann, L. W., Strom, K. M., et al. 1990, *AJ*, **99**, 869  
 Kospal, A. 2018, in 2018 ESO Meeting, Take a Closer Look, <https://www.eso.org/sci/meetings/2018/tcl2018/posters.html>  
 Kóspál, Á., Ábrahám, P., Csengeri, T., et al. 2017, *ApJ*, **843**, 45  
 Krijt, S., Schwarz, K. R., Bergin, E. A., et al. 2018, *ApJ*, **864**, 78  
 Ladd, E. F., Fuller, G. A., & Deane, J. R. 1998, *ApJ*, **495**, 871  
 Liu, H. B., Dunham, M. M., Pascucci, I., et al. 2018, *A&A*, **612**, A54  
 Liu, H. B., Mérand, A., Green, J. D., et al. 2019, *ApJ*, **884**, 97  
 Lodato, G., & Clarke, C. J. 2004, *MNRAS*, **353**, 841  
 Long, F., Pinilla, P., Herczeg, G. J., et al. 2018, *ApJ*, **869**, 17  
 Lorenzetti, D., Giannini, T., Larionov, V. M., et al. 2007, *ApJ*, **665**, 1182  
 Manara, C. F., Tazzari, M., Long, F., et al. 2019, *A&A*, **628**, A95  
 Mathieu, R. D., Martin, E. L., & Magazzu, A. 1996, AAS Meeting, **188**, 60.05  
 Mattila, K., Liljeström, T., & Toriseva, M. 1989, in *ESO Conf. Workshop Proc.* (Garching: ESO), 153  
 McMullin, J. P., Waters, B., Schiebel, D., Young, W., & Golap, K. 2007, in *ASP Conf. Ser.* 376, adass XVI, ed. R. A. Shaw, F. Hill, & D. J. Bell (San Francisco, CA: ASP), 127  
 Miotello, A., van Dishoeck, E. F., Williams, J. P., et al. 2017, *A&A*, **599**, A113  
 Moody, M. S. L., & Stahler, S. W. 2017, *A&A*, **600**, A133  
 Mottram, J. C., van Dishoeck, E. F., Kristensen, L. E., et al. 2017, *A&A*, **600**, A99  
 Pérez, S., Casassus, S., & Benítez-Llambay, P. 2018, *MNRAS*, **480**, L12  
 Pérez, S., Dunhill, A., Casassus, S., et al. 2015, *ApJL*, **811**, L5  
 Pérez, S., Hales, A., Liu, H. B., et al. 2020, *ApJ*, **889**, 59  
 Persi, P., Tapia, M., Gómez, M., et al. 2007, *AJ*, **133**, 1690  
 Principe, D. A., Cieza, L., Hales, A., et al. 2018, *MNRAS*, **473**, 879  
 Reipurth, B., & Aspin, C. 2010, in *Evolution of Cosmic Objects Through Their Physical Activity*, ed. H. A. Harutyunian, A. M. Mickaelian, & Y. Terzian (Yerevan: Gitutyun), 19  
 Reipurth, B., Aspin, C., & Herbig, G. H. 2012, *ApJL*, **748**, L5  
 Rosotti, G. P., Booth, R. A., Tazzari, M., et al. 2019, *MNRAS*, **486**, L63  
 Ruíz-Rodríguez, D., Cieza, L. A., Williams, J. P., et al. 2017a, *MNRAS*, **466**, 3519  
 Ruíz-Rodríguez, D., Cieza, L. A., Williams, J. P., et al. 2017b, *MNRAS*, **468**, 3266  
 Safron, E. J., Fischer, W. J., Megeath, S. T., et al. 2015, *ApJL*, **800**, L5  
 Samus, N. 2009, *CBET*, **1896**, 1  
 Schwarz, K. R., Bergin, E. A., Cleeves, L. I., et al. 2018, *ApJ*, **856**, 85  
 Semkov, E. H., Peneva, S. P., Munari, U., et al. 2013, *A&A*, **556**, A60  
 Sheehan, P. D., Wu, Y.-L., Eisner, J. A., et al. 2019, *ApJ*, **874**, 136  
 Simon, M., Dutrey, A., & Guilloteau, S. 2000, *ApJ*, **545**, 1034  
 Sipos, N., Ábrahám, P., Acosta-Pulido, J., et al. 2009, *A&A*, **507**, 881  
 Takami, M., Chen, T.-S., Liu, H. B., et al. 2019, *ApJ*, **884**, 146  
 Tazzari, M., Beaujean, F., & Testi, L. 2017, *galario: Gpu Accelerated Library for Analyzing Radio Interferometer Observations*, v1.2.2, Astrophysics Source Code Library, ascl:1710.022  
 Tazzari, M., Beaujean, F., & Testi, L. 2018, *MNRAS*, **476**, 4527  
 Thommes, J., Reipurth, B., Aspin, C., et al. 2011, *CBET*, **2795**, 1  
 Tobin, J. J., Sheehan, P., Megeath, S. T., et al. 2020, arXiv:2001.04468  
 Trapman, L., Facchini, S., Hogerheijde, M. R., et al. 2019, *A&A*, **629**, A79  
 Tripathi, A., Andrews, S. M., Birstiel, T., et al. 2017, *ApJ*, **845**, 44  
 Tripathi, A., Andrews, S. M., Birstiel, T., et al. 2018, *ApJ*, **861**, 64  
 Vorobyov, E. I., & Basu, S. 2015, *ApJ*, **805**, 115  
 Williams, J. P., & Best, W. M. J. 2014, *ApJ*, **788**, 59  
 Williams, J. P., & Cieza, L. A. 2011, *ARA&A*, **49**, 67  
 Wilson, T. L., & Rood, R. 1994, *ARA&A*, **32**, 191  
 Zhu, Z., Espaillat, C., Hinkle, K., et al. 2009, *ApJL*, **694**, L64  
 Zhu, Z., Hartmann, L., Gammie, C., et al. 2009, *ApJ*, **701**, 620  
 Zsidi, G., Ábrahám, P., Acosta-Pulido, J. A., et al. 2019, *ApJ*, **873**, 130  
 Zurlo, A., Cieza, L. A., Williams, J. P., et al. 2017, *MNRAS*, **465**, 834